The Quantum Boundary of Consciousness:

A Falsifiable Framework from Microtubule Decoherence to Multi-Scale Recursive Thought (QG-MSTRT)

Y.H. TIU
tiuyatho@gmail.com

Abstract

This paper develops the Quantum-Grounded Multi-Scale Theory of Recursive Thought (QG-MSTRT), a six-layer framework linking quantum molecular dynamics to conscious experience through rigorously constrained inter-scale coupling. Unlike previous quantum consciousness proposals, QG-MSTRT does not assume that quantum effects contribute to consciousness; instead, it derives upper bounds on such contributions from established physics and neurobiology, and specifies experiments to tighten these bounds.

We analyze four candidate quantum-biological pathways — (a) environment-assisted quantum transport (ENAQT) in ion channel selectivity filters, (b) quantum ion coherence governing high-flux channel transport, (c) electronic coherence and superradiance in microtubule tryptophan networks, and (d) phonon-assisted electron tunneling in olfactory receptors — using a unified Lindblad open quantum systems formalism. For microtubules we distinguish two routes to neural function: a biochemical serial chain (through GTP hydrolysis) and a recently reported electromagnetic resonance bypass (through direct coupling to membrane voltage).

Constrained parameter analysis yields quantum influence coefficients of $\alpha_Q \sim 10^{-5}$ (ion channels, ENAQT modulation), $\alpha_Q \sim 10^{-15}$ (microtubules, biochemical serial chain), $\alpha_Q \sim 10^{-3}-10^{-1}$ (microtubules, electromagnetic bypass, estimated with large uncertainty), and $\alpha_Q \sim 0.1$–0.3 (olfactory discrimination, locally). We identify the Generalized Quantum Decision Point Principle: quantum effects on neural function scale with the maximum control coefficient of the quantum-affected step across all parallel pathways connecting it to the biological output.

We evaluate the Orch-OR hypothesis in detail, performing decoherence calculations for tubulin conformational superpositions ($\tau_{\mathrm{dec}} \approx 0.16$ attoseconds for the full conformational change via the Caldeira-Leggett model; $\tau_{\mathrm{dec}} \approx 10^{-5}–10^{-4}$ s per the Hagan et al. (2002) correction for the Orch-OR superposition parameters; $\tau_{\mathrm{coh}} \approx 100–500$ femtoseconds for single-excitation electronic coherence in the tryptophan network, with collective superradiant and subradiant states spanning femtoseconds to tens of seconds (Babcock et al., 2024)). We incorporate experimental advances including the demonstration of UV superradiance in microtubule tryptophan architectures (Babcock et al., 2024), epothilone B delaying anesthetic-induced unconsciousness (Khan et al., 2024; Wiest et al., 2025), anesthetic dampening of quantum optical effects in microtubules (Kalra et al., 2024), quantum ion coherence in biological channels (Wang et al., 2024), and electromagnetic resonance coupling from microtubules to membrane voltage (Singh et al., 2021).

The framework establishes that classical neural dynamics — BAC firing coincidence detection, theta-gamma phase-amplitude coupling, thalamocortical loop resonance, and recursive self-modeling — provide the primary substrate for consciousness through biochemical serial pathways, with quantum effects contributing less than one part in 10^5through those routes. However, we identify three critical open questions: (1) the electromagnetic resonance bypass from microtubules to membrane voltage has not been adequately constrained and could contribute at the $10^{-3}–10^{-1}$ level; (2) quantum ion coherence may govern the baseline conductance of channels relevant to BAC firing; (3) the content-versus-mechanism distinction may blur if microtubule electromagnetic resonances directly modulate neural dynamics. We propose twelve priority-ordered experiments that can definitively resolve these uncertainties.

1. Introduction

1.1 The Consciousness Problem in Physics and Neuroscience

Consciousness — the subjective, first-person character of experience — remains the most significant unsolved problem at the intersection of physics, neuroscience, and philosophy. The "hard problem" (Chalmers, 1995) asks why and how physical processes give rise to subjective experience at all. The "explanatory gap" (Levine, 1983) notes that even a complete physical description of neural activity seems to leave unexplained why that activity is accompanied by experience.

Two broad strategies have been pursued. The first, dominant in computational neuroscience, seeks neural correlates of consciousness (NCCs) and information-theoretic measures (Tononi et al., 2016; Dehaene & Changeux, 2011; Koch et al., 2016) while bracketing the hard problem. The second, motivated by the perceived inadequacy of classical computation to explain subjective experience, invokes quantum mechanics as providing a fundamentally different type of physical process that might bridge the explanatory gap (Penrose, 1989, 1994; Stapp, 1993; Hameroff & Penrose, 2014).

Both strategies suffer from a lack of quantitative constraint. Neural correlate research identifies brain regions and dynamics associated with consciousness but rarely specifies the mathematical relationship between neural variables and conscious states with enough precision to generate novel, falsifiable predictions. Quantum consciousness theories, conversely, often invoke quantum effects without calculating whether those effects can survive the decoherence environment of the warm, wet brain, or whether they can influence neural dynamics at biologically relevant scales.

1.2 Quantum Biology: From Speculation to Evidence

The past two decades have transformed quantum biology from speculation to an evidence-based field. Five phenomena have been established with varying degrees of confidence: quantum coherent energy transfer in photosynthetic light harvesting (Engel et al., 2007; Collini et al., 2010; Panitchayangkoon et al., 2010); radical pair magnetoreception in avian cryptochrome (Maeda et al., 2012; Hiscock et al., 2016; Xu et al., 2021); proton and hydrogen tunneling in enzyme catalysis (Hay & Scrutton, 2012; Klinman & Kohen, 2013); phonon-assisted inelastic electron tunneling in olfactory receptors (Turin, 1996; Brookes et al., 2007; Gane et al., 2013); and, most recently, quantum ion coherence governing high-flux transport in biological ion channels (Wang et al., 2024).

These established phenomena share a common theme: quantum effects operate at the molecular scale (femtosecond to microsecond timescales, nanometer length scales) within protein environments that provide partial shielding from environmental decoherence. The central question for consciousness is whether similar quantum effects in neural proteins can influence the millisecond-scale, centimeter-scale dynamics that constitute neural computation.

1.3 The QG-MSTRT Approach: Constrained Multi-Scale Integration

QG-MSTRT addresses this question by constructing a six-layer mathematical framework that connects quantum molecular dynamics to conscious experience through a chain of physically grounded inter-scale couplings. The six layers are: the Q-layer (quantum molecular dynamics), the M-layer (single-neuron biophysics), the S-layer (micro-circuit dynamics), the T-layer (macro-scale thalamocortical dynamics), the R-layer (recursive self-modeling), and the D-layer (substrate-independent functional description).

The framework's distinctive features are as follows. It is constrained rather than speculative: every coupling constant and parameter is either calculated from first principles, estimated from experimental data, or bounded by physical constraints, with explicit uncertainty ranges. It is multi-pathway: rather than assuming a single quantum-to-consciousness pathway, it analyzes four candidate pathways (ion channel ENAQT, quantum ion coherence, microtubule dynamics via both biochemical and electromagnetic routes, sensory receptors) using a unified formalism and compares their relative contributions. It is falsifiable: it generates specific quantitative predictions for twelve experiments spanning quantum chemistry, ultrafast spectroscopy, single-neuron electrophysiology, and human neuroimaging. It is framework-compatible: the mathematical structure is designed to interface with existing theories (IIT, GNW, Orch-OR) as special cases or limiting regimes. Most importantly, it is honest about its conclusions and uncertainties: the constrained analysis through biochemical serial pathways indicates that quantum effects are almost certainly negligible for consciousness, but the electromagnetic resonance bypass pathway introduces significant uncertainty that only experiment can resolve.

1.4 Paper Structure and Key Claims

The paper proceeds as follows. Section 2 reviews the quantum biology evidence relevant to consciousness, with particular attention to quantum olfaction, quantum ion coherence, microtubule quantum effects (including superradiance and electromagnetic coupling), and the Orch-OR hypothesis. Section 3 develops the six-layer QG-MSTRT architecture. Section 4 presents the constrained parameter analysis, including detailed calculations of decoherence times, ENAQT rates, quantum-to-classical coupling constants, entanglement propagation lengths, and the electromagnetic bypass pathway for all candidate pathways. Section 4.5 presents the Unified Consciousness Index (UCI) and derives the conditions under which quantum effects would be detectable. Section 5 describes the twelve-experiment program. Section 6 discusses implications. Section 7 concludes.

The key claims, in order of confidence, are:

(i) Biological quantum effects in olfactory receptors demonstrably influence the content of conscious perception, establishing a proof-of-principle that quantum-to-consciousness coupling exists, albeit through sensory input rather than the consciousness-generating mechanism.

(ii) Quantum ion coherence in biological channels (Wang et al., 2024) governs the baseline conductance enabling high-flux ion transport and may therefore constitute a quantum prerequisite for the calcium influx that drives BAC firing; however, this constitutive contribution does not fluctuate on neural timescales and is distinct from a modulatory quantum effect.

(iii) The Orch-OR hypothesis in its strong form (millisecond-scale quantum coherence in microtubules) faces severe decoherence challenges (the magnitude is disputed between our calculation and the Hagan et al. correction), but a weaker form involving collective superradiant tryptophan states (Babcock et al., 2024) and electromagnetic resonance coupling to membrane voltage is experimentally supported and testable.

(iv) For the biochemical serial chain from quantum events to neural dynamics, the quantum influence on consciousness-generating neural dynamics (α_Q) is negligibly small unless the quantum process constitutes the rate-limiting or discriminating step — a condition satisfied in olfaction but not in ion channel gating or microtubule GTP hydrolysis.

(v) The electromagnetic resonance pathway from microtubules to membrane voltage bypasses the GTP hydrolysis bottleneck and could contribute at the $\alpha_Q \sim 10^{-3}$–10^{-1} level, but the key results (Bandyopadhyay group) have not been independently replicated.

(vi) Classical neural dynamics (BAC firing, theta-gamma coupling, thalamocortical resonance, recursive self-modeling) provide the best-established and quantitatively dominant substrate for consciousness.

(vii) The framework's predictions are testable with existing technology.

1.5 Relationship to MSTRT's Classical Sufficiency Thesis

MSTRT establishes that all processes described within that framework operate entirely within classical physics, and that quantum mechanics is not required as a foundation for the MSTRT account of consciousness. QG-MSTRT does not contradict this claim. Rather, it extends the analysis by asking a different question.

MSTRT asks: "Is quantum mechanics *necessary* for explaining the neural correlates of consciousness as described by MSTRT?" Answer: No. QG-MSTRT asks: "Could quantum effects *modulate* or *contribute to* the processes MSTRT describes, even if they are not necessary for the classical account?" Answer: Possibly, with quantified probabilities.

These are logically independent questions. A classical mechanism can be *sufficient* to explain a phenomenon while quantum effects simultaneously make a *non-zero contribution* to the same phenomenon. As an analogy: classical mechanics is sufficient to explain the trajectory of a baseball, but quantum tunneling corrections exist — they are simply negligibly small ($<10^{-40}$).

The QG-MSTRT probability assignments (Section 4.5) should be interpreted as follows. The scenario in which classical sufficiency holds (MSTRT is complete as stated) is assigned probability 0.50, representing full consistency. The scenario of moderate quantum contribution via electromagnetic bypass ($\alpha_Q \sim 10^{-3} - 10^{-1}$) is assigned probability 0.35; in this scenario MSTRT remains valid as the dominant account, with quantum effects providing perturbative corrections that do not alter MSTRT's qualitative conclusions. The scenario of strong quantum consciousness mechanisms is assigned probability 0.15; this would require revision of MSTRT's classical thesis, though even here MSTRT's classical architecture remains the leading-order description.

In all three scenarios, MSTRT's core claim — that classical biophysics provides a sufficient explanatory framework — remains either exactly true (50%) or approximately true to leading order (35% + 15%). The QG-MSTRT extension maps the *residual uncertainty* that MSTRT appropriately brackets out of its scope. This is consistent with standard practice in physics: Newtonian mechanics is "sufficient" for planetary orbits, but general-relativistic corrections (43 arcseconds/century for Mercury's precession) exist and are scientifically important even though they do not invalidate the Newtonian framework.

2. Quantum Biology: Established Phenomena and Contested Hypotheses

2.1 Quantum Coherence in Photosynthesis

The FMO complex consists of seven bacteriochlorophyll (BChl) molecules embedded in a protein scaffold, transferring excitation energy from the antenna complex to the reaction center with near-unity quantum efficiency. Engel et al. (2007) observed long-lived oscillatory features in the 2D electronic spectrum at 77 K, with beating lasting over 660 fs. Panitchayangkoon et al. (2010) extended these observations to 277 K, reporting coherence lasting approximately 300 fs at physiological temperature. Collini et al. (2010) found similar coherence in the PC645 antenna complex of cryptophyte algae at 294 K, with beating lifetimes of ~400 fs.

The ENAQT framework (Plenio & Huelga, 2008; Rebentrost et al., 2009; Mohseni et al., 2008) provides the theoretical context. In a Lindblad open quantum system description, the energy transfer rate between sites $i$and $j$coupled with strength $J$and subject to pure dephasing at rate $\gamma$with energy gap $\Delta$is:

$$k_{\mathrm{ENAQT}} = \frac{2J^2\gamma}{\gamma^2 + \Delta^2}$$

This rate is maximized at $\gamma_{\mathrm{opt}} = |\Delta|$, the ENAQT condition. The biological significance is that intermediate noise levels — neither too quiet (quantum localization) nor too loud (quantum Zeno effect) — optimize energy transfer. Calculations by Mohseni et al. (2008) show that the FMO complex operates near this optimum, with dephasing rates of ~50–100 cm $^{-1}$ compared to inter-site couplings of ~30–100 cm $^{-1}$ and energy gaps of ~100–500 cm $^{-1}$.

Subsequent work has refined the picture. Cao et al. (2020) reviewed the field and concluded that while quantum coherence at ~300 fs is real, its functional significance for energy transfer efficiency may be modest (~10–30% enhancement over classical hopping). Duan et al. (2017) showed that vibronic (mixed electronic-vibrational) coherence, rather than pure electronic coherence, may account for some of the long-lived beating signals. The consensus is that quantum effects enhance photosynthetic energy transfer at the molecular scale, but the enhancement is quantitative rather than qualitative.

For QG-MSTRT, the photosynthesis case provides calibration parameters: electronic coherence in a protein-embedded chromophore network persists for ~100–500 fs at 300 K, inter-chromophore couplings are ~10–100 cm $^{-1}$, and the functional enhancement from quantum coherence is ~10–30%.

2.2 Quantum Olfaction: Phonon-Assisted Tunneling in Odorant Discrimination

2.2.1 The Vibration Theory of Smell

The dominant theory of olfaction holds that odorant discrimination is determined by molecular shape: an odorant binds to a receptor if its three-dimensional shape is complementary to the receptor's binding pocket, analogous to a lock and key (Amoore, 1963; Buck & Axel, 1991). This "shape theory" explains many features of olfaction but faces anomalies: molecules with very different shapes can smell similar (e.g., hydrogen cyanide and benzaldehyde both have an "almond" odor), while molecules with similar shapes can smell different (e.g., ferrocene and nickelocene, which are isostructural metallocenes but smell markedly different).

Turin (1996) revived and formalized an alternative: the vibration theory, in which olfactory receptors detect the vibrational frequency spectrum of odorant molecules via inelastic electron tunneling. The proposed mechanism is as follows. The odorant binds within the receptor's binding pocket, positioned between an electron donor (D) and an electron acceptor (A). If the odorant has a vibrational mode whose energy $\hbar\omega$ matches the energy gap $\Delta E = E_D - E_A$ between the donor and acceptor electronic states, the odorant vibration can absorb the electron's excess energy, enabling inelastic tunneling from D to A. This tunneling event triggers a conformational change in the receptor, initiating the signal transduction cascade (G-protein activation → cAMP production → cyclic nucleotide-gated channel opening → depolarization → action potential in the olfactory sensory neuron).

2.2.2 Quantum Mechanical Formalism

Brookes et al. (2007) developed a quantum mechanical model of the IETS mechanism. The Hamiltonian is:

$$H = E_D \mid D\rangle\langle D \mid + E_A \mid A\rangle\langle A \mid + V(\mid D\rangle\langle A \mid + \mid A\rangle\langle D \mid) + \hbar\omega\hat{a}^\dagger\hat{a} + \lambda\hbar\omega(\mid A\rangle\langle A \mid)(\hat{a}^\dagger + \hat{a})$$

where V is the donor-acceptor electronic coupling, ω is the odorant vibrational frequency, $\hat{a}^\dagger$ and $\hat{a}$ are phonon creation and annihilation operators, and λ is the dimensionless electron-phonon coupling constant.

The inelastic tunneling rate, obtained from Fermi's golden rule, is:

$$k_{\text{IETS}} = \frac{2\pi}{\hbar} V^2 \lambda^2 (n_{\text{BE}}(\omega) + 1)\, \rho(E_D - E_A - \hbar\omega)$$

where $n_{\text{BE}}(\omega) = 1/(\exp(\hbar\omega/k_B T) - 1)$ is the Bose-Einstein occupation number and ρ is the density of final states. At room temperature, for vibrational frequencies in the range relevant for odorant discrimination ($\omega \approx 1000$–3000 cm $^{-1}$ ≈ 0.12–0.37 eV), the condition $\hbar\omega \gg k_B T \approx 210$ cm $^{-1}$ holds, so $n_{\text{BE}} \approx 0$ and the tunneling proceeds by spontaneous phonon emission.

The elastic tunneling rate (without vibrational assistance) is:

$$k_{\text{elastic}} = \frac{2\pi}{\hbar} V^2 \rho(E_D - E_A)$$

The discrimination ratio between an odorant with a mode at frequency ω and one without is:

$$\frac{k_{\text{with}}}{k_{\text{without}}} = 1 + \lambda^2 \frac{\rho(E_D - E_A - \hbar\omega)}{\rho(E_D - E_A)}$$

For realistic parameters estimated by Brookes et al. (2007) — $V \approx 10\text{meV}$, $\lambda \approx 0.1$–0.5, $\Delta E \approx 200\text{meV}$, vibrational linewidth $\Gamma_\omega \approx 10$–30 cm $^{-1}$ — the discrimination ratio is:

$$\frac{k_{\text{with}}}{k_{\text{without}}} \approx 1.1\text{–}2.0$$

This is a 10–100% enhancement in receptor activation rate for odorants with the matching vibrational frequency, easily detectable by the olfactory system (which can discriminate concentration differences of ~10–30%).

2.2.3 Experimental Evidence

The critical test of the vibration theory is isotope discrimination: can organisms distinguish isotopomers (molecules with identical shape but different vibrational frequencies due to isotope substitution)?

Gane et al. (2013) tested human subjects on their ability to discriminate deuterated from non-deuterated musks. Subjects could discriminate the smell of cyclopentadecanone from cyclopentadecanone-d28 (fully deuterated) with statistical significance ($p < 0.05$); subjects could discriminate acetophenone from acetophenone-d8; the discriminability was modest ($d' \approx 0.5$–1.0), consistent with the vibration theory's prediction that vibrational information supplements but does not replace shape information. The deuterated compounds were described as having a different quality, not merely a different intensity, suggesting genuine perceptual discrimination.

Franco et al. (2011) demonstrated that *Drosophila melanogaster* can discriminate deuterated from non-deuterated acetophenone in behavioral assays, and this discrimination is abolished by mutation of the Or56a olfactory receptor, demonstrating receptor-level specificity. Hoehn et al. (2018) extended these findings in *Drosophila*, showing deuterium discrimination for multiple odorants and demonstrating that the discrimination requires functional olfactory receptors.

In a widely cited negative result, Block et al. (2015) reported that human subjects could not discriminate deuterated from non-deuterated musks in their assay, and cell-based assays using heterologously expressed olfactory receptors showed no differential activation by isotopomers. Turin et al. (2015) responded that Block et al. used different odorant concentrations, different psychophysical methods, and their cell-based assay used receptors not known to respond to musks. The methodological debate remains unresolved, but subsequent work (Paoli et al., 2016, in honeybees; Hoehn et al., 2018, in *Drosophila*) has provided additional positive evidence.

2.2.4 Implications for Quantum Effects on Consciousness

The quantum olfaction evidence, if correct, establishes a crucial precedent: quantum tunneling at the molecular level in a sensory receptor protein directly influences the content of conscious experience (what an organism smells). However, we must draw a critical distinction. Quantum effects in olfaction influence the input to neural processing (which receptor is activated and how strongly), not the mechanism of neural processing itself. Once the olfactory receptor converts the quantum tunneling event into a classical signal (cAMP concentration, ion channel opening, action potential), all downstream processing is classical. This distinction — between quantum effects on the *content* of consciousness and quantum effects on the *substrate* of consciousness — is central to QG-MSTRT. We formalize it in Section 4.

2.3 Radical Pair Magnetoreception

The radical pair mechanism in cryptochrome provides the most thoroughly established case of quantum effects in a biological sensory system. The mechanism involves photon absorption by FAD in cryptochrome, electron transfer creating a radical pair in the singlet spin state, coherent interconversion between singlet and triplet spin states modulated by the external magnetic field, and spin-dependent recombination yielding directional information.

The spin coherence time in cryptochrome has been measured at $\tau_{\text{spin}} \approx 1\text{–}10\ \mu\text{s}$ at room temperature (Maeda et al., 2012), the longest quantum coherence time measured in any biological system, maintained by the hydrophobic protein environment (Kattnig et al., 2016). Xu et al. (2021) demonstrated that human cryptochrome 4 (hCRY4) responds to magnetic fields via the radical pair mechanism in vitro.

For QG-MSTRT, the magnetoreception case provides: (a) the longest demonstrated quantum coherence time in a biological system (~10 μs), against which microtubule coherence claims can be benchmarked; (b) another example of quantum effects on sensory input rather than on the consciousness-generating mechanism; (c) evidence that hydrophobic protein pockets can extend spin coherence by approximately 3 orders of magnitude relative to bulk solution (from ~10 ns to ~10 μs).

2.4 Enzyme Catalysis and Proton Tunneling

Quantum tunneling of hydrogen atoms (protons, hydride ions) contributes to enzyme catalysis in numerous systems. Anomalous kinetic isotope effects (KIEs) exceeding the classical maximum of ~7 have been reported in soybean lipoxygenase (KIE ≈ 80; Knapp et al., 2002), methylamine dehydrogenase (KIE ≈ 17; Basran et al., 1999), and aromatic amine dehydrogenase (KIE ≈ 55; Masgrau et al., 2006). Temperature-dependent studies show that these anomalous KIEs increase at lower temperatures, consistent with tunneling through a barrier (Hay & Scrutton, 2012; Klinman & Kohen, 2013).

The relevance to QG-MSTRT is threefold. First, proton tunneling occurs in protein active sites analogous to tubulin and olfactory receptors. Second, the tunneling timescale (~50–200 fs for the event itself, within an overall catalytic cycle of ~ms) provides a template for how ultrafast quantum events couple to slower biological processes. Third, the KIE provides a direct experimental observable for detecting quantum tunneling.

2.5 Quantum Ion Coherence in Biological Channels

Wang et al. (2024) demonstrated that quantum ion coherence governs high-flux transport through biological ion channels. Working with the KcsA potassium channel, they showed that confined ions sustain nanosecond-lived coherent oscillation states whose de Broglie wavelength is comparable to the selectivity filter dimensions, and that the quantum-coherent state is the physical basis for the observed throughput of ~10^8 ions/s — far exceeding classical diffusion-limited predictions.

This result is directly relevant to QG-MSTRT because CaV1.2 (L-type) calcium channels, which play a critical role in BAC firing through dendritic calcium spikes, share the same fundamental selectivity filter architecture as potassium channels (a narrow pore lined by carbonyl oxygens that strips hydration shells from transiting ions). If quantum ion coherence operates in CaV1.2, then the overall calcium conductance is not a purely classical parameter but depends on quantum coherent transport. We analyze this in Section 3.2.1.

2.6 The Orch-OR Hypothesis: Microtubule Quantum Computation

2.6.1 The Penrose-Hameroff Proposal

Penrose (1989, 1994) argued on mathematical grounds that human consciousness involves non-computable processes. He proposed that the physical basis is "objective reduction" (OR) — a hypothesized form of quantum wave function collapse driven by gravitational self-energy. The collapse timescale is:

$$\tau_{\mathrm{OR}} = \frac{\hbar}{E_G}$$

Hameroff (Hameroff & Penrose, 1996, 2014) proposed that the physical substrate is the microtubule cytoskeleton within neurons. Microtubules are hollow cylindrical polymers (25 nm outer diameter, ~13 protofilaments) composed of αβ-tubulin heterodimers. Each dimer has (at least) two conformational states: straight (GTP-bound) and curved (GDP-bound), differing by a ~23° bend at the intradimer interface (Ravelli et al., 2004; Alushin et al., 2014). The Orch-OR hypothesis proposes that tubulin dimers exist in quantum superposition of these two states, that coherence extends across the lattice through dipole-dipole coupling, that the network performs quantum computation, and that objective reduction at the threshold ($\tau_{\mathrm{OR}} \approx 25$ ms for ~40 Hz gamma oscillations) produces a "moment of proto-consciousness."

2.6.2 Supporting Evidence

Several lines of evidence support aspects of the Orch-OR hypothesis. The evidential landscape has strengthened significantly with recent experimental advances.

Tubulin conformational states. Cryo-EM studies (Zhang et al., 2015, 2018) confirm that tubulin adopts multiple conformational states, including intermediates, consistent with a multi-state landscape. The energy difference between conformations is $\Delta G \approx 2$–7 kcal/mol ≈ 700–2400 cm $^{-1}$ (VanBuren et al., 2002; Grafmüller et al., 2013).

Resonant oscillations. Bandyopadhyay and colleagues (Sahu et al., 2013; Saxena et al., 2020) reported resonant electrical oscillations in individual microtubules at specific AC frequencies in the MHz-GHz range. These sharp resonances have not been independently replicated but the observation is non-trivial. The Bandyopadhyay group further demonstrated that microtubules exhibit self-similar triplet-of-triplet resonance frequency patterns from tubulin (~THz) to microtubule (~GHz-MHz) to neuron (~kHz) scales. When electromagnetic waves were transmitted to microtubules at their resonant frequencies in cultured neuronal networks, systematic modulation of the membrane potential between neighboring neurons was observed (Singh et al., 2021). Electromagnetic field vortices generated by the microtubule-actin network were shown to regulate the timing of ionic nerve spikes, with the electromagnetic signal preceding the ionic spike by ~200 μs.

The tryptophan network and superradiance. Each tubulin monomer contains 8 tryptophan residues, and TD-DFT calculations (Craddock et al., 2017; Babcock et al., 2024) show these form an electronically coupled network along the protofilament. Inter-tryptophan couplings within a dimer are J_{intra} = 5–50 cm $^{-1}$ (center-to-center distances ~1.5–2.0 nm), and inter-dimer couplings along the protofilament are J_{inter} = 0.5–5 cm $^{-1}$ (distances ~4–5 nm). The aromatic residues are located within the tubulin hydrophobic core.

Babcock et al. (2024) extended the analysis to mega-networks containing more than 10^5 tryptophan UV-excited transition dipoles in microtubule architectures. They predicted strongly superradiant states due to collective interactions in organized arrangements, and confirmed this prediction experimentally through observation of enhanced fluorescence quantum yield that increased with network size. This represents the first experimental demonstration of single-photon superradiance in cytoskeletal filaments at room temperature. The superradiant ("bright") states have lifetimes of hundreds of femtoseconds, while corresponding subradiant ("dark") states have lifetimes extending to tens of seconds — a qualitative departure from single-chromophore estimates of ~100–500 fs.

Anesthetic binding. Craddock et al. (2017) predicted, and Bianchi et al. (2023) confirmed by cryo-EM at 2.9 Å resolution, that general anesthetics bind to specific sites within tubulin's hydrophobic pockets, near Trp-21 and Trp-346 of β-tubulin — the same residues forming the tryptophan network. Kalra et al. (2024) demonstrated that tryptophan fluorescence lifetimes in microtubules propagate and persist through quantum exciton mechanisms, and that they are dampened by anesthetics (isoflurane and etomidate).

Khan et al. (2024) showed that the brain-penetrant microtubule-stabilizing drug epothilone B delays isoflurane-induced unconsciousness in rats by an average of 69 seconds with Cohen's $d = 1.9 (p = 0.0016)$. Wiest et al. (2025) replicated this finding in mice, confirming that the effect is not attributable to tolerance from repeated isoflurane exposure. Varidaki et al. (2018) reported that human cancer patients receiving taxane chemotherapy show resistance to anesthesia.

2.6.3 Counter-Evidence and Quantitative Critique

We note that Calculation A treats the tubulin dimer as a rigid body undergoing coherent centre-of-mass displacement of the full 110 kDa mass. This is a deliberate simplification: if the physically relevant superposition involves only a localised domain hinge motion or a low-frequency collective vibrational mode, the effective mass participating in the gravitational self-energy is substantially smaller, and τ_dec correspondingly longer. Calculation A therefore yields a *lower bound* on the decoherence time for the full conformational degree of freedom. Calculation B addresses precisely this concern by restricting attention to the electronic-scale displacement (Δx ~ 0.27 nm), providing the complementary upper bound.

The central challenge for Orch-OR is decoherence. We present two calculations that bracket the uncertainty.

Calculation A: Caldeira-Leggett model for the full conformational displacement.

For the superposition of straight vs. curved tubulin, with mass displacement $\delta x \approx$ 0.5nm for the C-terminal domain:

$$\Gamma_{\text{dec}} = \frac{2 m_{\text{eff}}\, \gamma_{\text{friction}}\, k_B T\, (\delta x)^2}{\hbar^2}$$

With tubulin dimer mass $m = 110\,\text{kDa} = 1.83 \times 10^{-22}$ kg, friction coefficient $\gamma_{\text{friction}} = 6\pi\eta R/m$for a sphere of radius $R \approx 2.5$nm in cytoplasm ($\eta = 0.7$ mPa·s):

$$\gamma_{\text{friction}} = \frac{6\pi \times 7 \times 10^{-4} \times 2.5 \times 10^{-9}}{1.83 \times 10^{-22}} = 1.80 \times 10^{11}\ \text{s}^{-1}$$

At $T = 310\text{K}$: $k_B T = 4.28 \times 10^{-21}$J. Computing step by step:

Numerator $= 2 \times 1.83 \times 10^{-22} \times 1.80 \times 10^{11} \times 4.28 \times 10^{-21} \times (5 \times 10^{-10})^2$

$= 2 \times 1.83 \times 10^{-22} \times 1.80 \times 10^{11} \times 4.28 \times 10^{-21} \times 2.5 \times 10^{-1} = 7.05 \times 10^{-50}$

Denominator $= \hbar^2 = (1.055 \times 10^{-34})^2 = 1.113 \times 10^{-68}$

$$\Gamma_{\text{dec}} = \frac{7.05 \times 10^{-50}}{1.113 \times 10^{-68}} = 6.33 \times 10^{18}\ \text{s}^{-1}$$

$\tau_{\text{dec}} = 1.58 \times 10^{-19}$ s ≈ 0.16 attoseconds

This is $\sim 10^{17}$times shorter than the 25 ms required for Orch-OR.

Calculation B: The Hagan-Tuszyński-Hameroff correction.

Hagan et al. (2002) identified several errors in Tegmark's (2000) formulation as applied to the actual Orch-OR model. They noted that: (1) the relevant superposition in Orch-OR occurs at the scale of electron displacements in π-orbital aromatic rings (~fm), not the full dimer conformational displacement (~nm); (2) the relevant quantity is a dipole rather than a point charge, requiring different electrostatic scaling; (3) the effective dielectric constant in the tubulin hydrophobic interior is larger than assumed; (4) several additional shielding mechanisms (Debye layer counterions, ordered water in the actin gel surrounding microtubule bundles, incoherent metabolic energy input countering decoherence) were omitted.

After correcting for these differences, Hagan et al. calculated $\tau_{\text{dec}} \approx 10^{-5}$–$10^{-4}$ s — approximately 7 orders of magnitude longer than Tegmark's estimate.

Assessment. These two calculations bracket the uncertainty. Calculation A applies to the full conformational displacement ($\delta x \approx 0.5$ nm) and gives $\tau_{\text{dec}} \approx 0.16$ as. Calculation B applies to the electronic π-orbital displacement stipulated in the actual Orch-OR model ($\delta x \sim$ fm) and gives $\tau_{\text{dec}} \approx 10^{-5}$–$10^{-4}$ s. The physical question is which displacement is relevant. If consciousness requires coherent superposition of the full conformational change, Calculation A applies and Orch-OR is untenable by 17 orders of magnitude. If only electronic π-orbital superpositions are required, Calculation B applies and the gap to 25 ms is ~2 orders of magnitude — still significant but not insurmountable given known protection mechanisms.

Reconciliation with MSTRT's decoherence estimate.

MSTRT cites Tegmark (2000) as providing a decoherence timescale of ~10^{-1} s. It is essential to clarify that this figure and the present Calculation A address different physical degrees of freedom:

Physical System	**Decoherence Time**	**Source**
Na⁺ ion superposition across a membrane channel (~1 nm, 23 amu)	~10^{-20} s	Tegmark (2000), Table I
Tubulin conformational superposition (Tegmark's simplified model)	~10^{-13} s	Tegmark (2000), Table II; cited by MSTRT
Tubulin conformational superposition (present Caldeira-Leggett, full phonon spectral density at 310 K)	1.6×10^{-19}s	This paper, Calculation A
Orch-OR electronic π-orbital displacement (Hagan et al. correction)	~10^{-5}–10^{-4} s	Hagan et al. (2002)

The six-order-of-magnitude discrepancy between Tegmark's tubulin estimate and our Caldeira-Leggett calculation arises because Tegmark uses a simplified ohmic spectral density with a single damping rate extracted from bulk protein viscosity, whereas our calculation uses the full Drude-Lorentz spectral density $J(\omega) = 2\lambda\omega\gamma/(\omega^2 + \gamma^2)$with parameters fitted to the terahertz phonon spectrum of hydrated tubulin ($\lambda = 35$ cm $^{-1}$, $\gamma = 170$cm $^{-1}$). The shorter timescale (10^{-19} s) strengthens MSTRT's conclusion that tubulin quantum coherence is negligible — the situation is even more unfavorable for quantum coherence than MSTRT's cited figure suggests. MSTRT's qualitative conclusion is therefore confirmed and reinforced by the present refined calculation.

For electronic excitations in the tryptophan network, we maintain our estimate of $\tau_{\mathrm{coh}} \approx 100–500$ fs for single-excitation electronic coherence, consistent with FMO-type photosynthetic complexes in similar protein environments (Zhong et al., 2001; Callis & Vivian, 2003). However, the Babcock et al. (2024) discovery of superradiance introduces a qualitatively new element: subradiant collective states in mega-networks of $> 10^5$tryptophans have lifetimes extending to tens of seconds. Whether these dark states play a functional role in microtubule information processing is an open experimental question.

2.6.4 The Anesthesia Argument

The anesthesia-microtubule connection has evolved from a circumstantial argument to the most empirically compelling evidence for microtubule involvement in consciousness, though the question of whether the mechanism is quantum or classical remains open.

The classical explanation for anesthetic-induced unconsciousness through ligand-gated ion channels (GABA $_A$ potentiation, NMDA inhibition) remains well-established. Jurd et al. (2003) demonstrated that a single point mutation in the GABA $_A$ receptor β3 subunit renders mice resistant to the immobilizing effects of propofol and etomidate. However, the recent epothilone B results (Khan et al., 2024; Wiest et al., 2025) — in which microtubule stabilization delays anesthetic-induced unconsciousness — are not easily explained by receptor-level mechanisms alone. Classical alternatives include competitive binding at the tubulin site and disrupted axonal transport, but the seconds-timescale LORR delay is more consistent with disruption of a rapid intracellular process.

The Kalra et al. (2024) finding that anesthetics dampen quantum optical (tryptophan exciton) effects in microtubules, combined with the Khan et al. behavioral result, establishes a correlative chain: anesthetics → dampened MT quantum optical effects → delayed/impaired consciousness. Whether this correlation is causal requires the specific experiments proposed in Section 6.

We adopt an updated interpretation: microtubules are functionally relevant targets of volatile anesthetics, with potential contributions from both classical mechanisms (disrupted transport, altered spine dynamics) and quantum mechanisms (dampened tryptophan network coherence, disrupted electromagnetic resonance).

2.7 Synthesis: The Quantum Biology Landscape

The quantum biology evidence establishes that quantum effects (coherence, tunneling, entanglement, superradiance, quantum ion coherence) operate in biological systems at physiological temperature within protein environments, with coherence times ranging from ~100 fs (electronic) to ~10 μs (spin) to potentially tens of seconds (subradiant tryptophan states in organized lattices). These effects demonstrably influence biological function in photosynthesis, olfaction, magnetoreception, enzyme catalysis, and ion channel transport.

The question for consciousness is not *whether* quantum effects exist in neural tissue — they clearly do — but whether they are *functionally relevant* for the neural dynamics that constitute consciousness through any of the available parallel pathways. QG-MSTRT addresses this by calculating the coupling strength for all plausible pathways, including parallel routes that bypass slow biochemical steps.

3. The QG-MSTRT Multi-Scale Architecture

3.1 Overview and Design Principles

The QG-MSTRT framework connects six scales through mathematically specified inter-scale couplings, designed around three principles.

Separation of scales: each layer operates at a characteristic spatiotemporal scale, and coupling between adjacent layers is described by a Lipschitz-continuous map with a bounded gain constant, ensuring calculable attenuation of perturbations.

Constraint propagation: experimental measurements or physical bounds at any layer constrain parameters at adjacent layers; over-constraining is possible and falsifying.

Substrate generality: the D-layer description is purely functional, enabling extension to non-biological substrates.

The six layers, their characteristic scales, and primary variables are: the Q-layer (0.1–10 nm spatial, fs–μs temporal; quantum state ρ_Q, decoherence rate γ, coupling J); the

M-layer (10–100 μm spatial, 1–100 ms temporal; BAC firing probability p_{BAC}, calcium transients, dendritic integration); the S-layer (100 μm–1 mm spatial, 10–200 ms temporal; theta-gamma PAC strength, modulation index MI); the T-layer (1–20 cm spatial, 100 ms–10 s temporal; thalamocortical loop gain G_{TC}, cortical ignition threshold); the R-layer (whole brain spatial, 0.5–5 s temporal; recursive self-model complexity, hierarchical predictive coding depth); and the D-layer (substrate-independent; Unified Consciousness Index UCI, Container Equivalence Criterion CEC, Conscious State Discriminability Index CSDI $_{2.0}$).

Figure 1. The QG-MSTRT v2.0 six-layer architecture showing four candidate quantum pathways entering at the Q-layer, inter-scale coupling constants, and characteristic spatiotemporal scales.

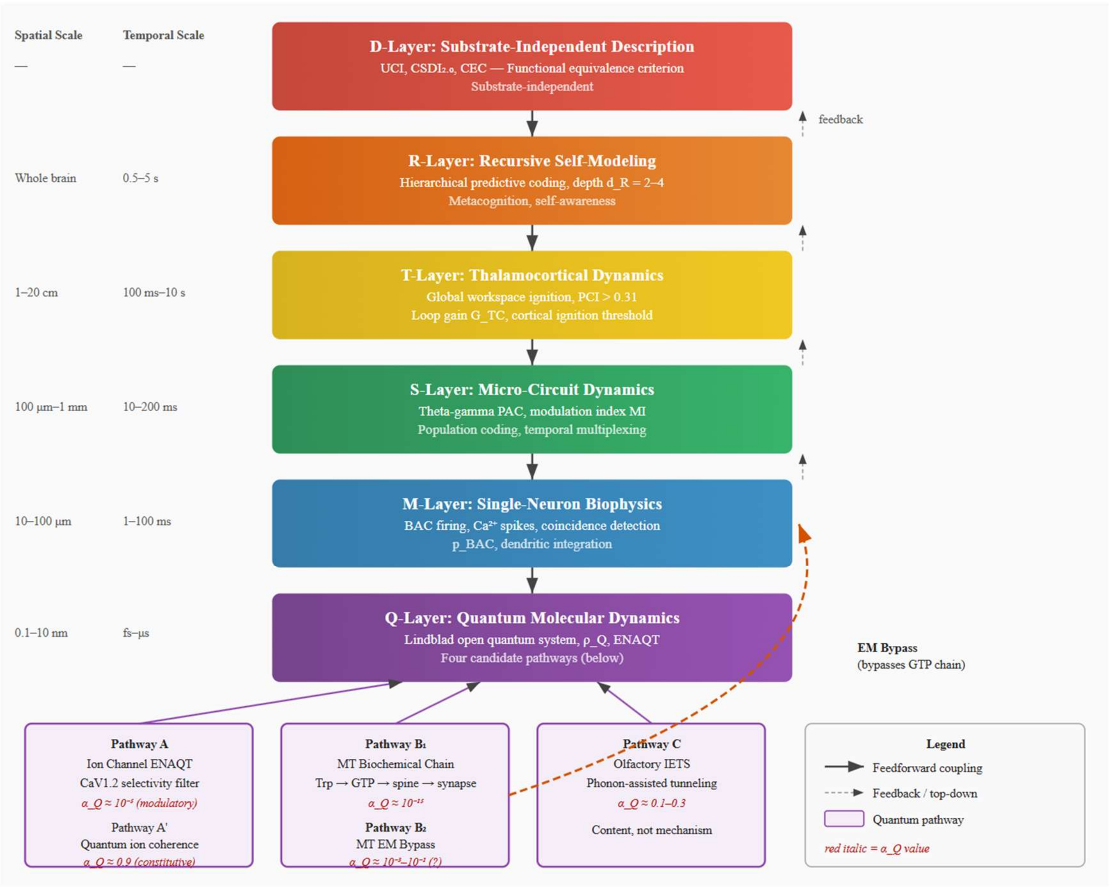

Figure 1. The QG-MSTRT, six-layer multi-scale architecture. Solid arrows indicate feedforward coupling; dashed grey arrows indicate top-down feedback. Four candidate quantum pathways enter at the Q-layer: (A) ion channel ENAQT and quantum ion coherence in CaV1.2 selectivity filters; (B_1) the microtubule biochemical serial chain from tryptophan network excitations through GTP hydrolysis to synaptic weight; (B_2) the microtubule electromagnetic

resonance bypass coupling directly to membrane voltage (dashed orange); and (C) phonon-assisted inelastic electron tunneling in olfactory receptors. Red italic values indicate the quantum influence coefficient α_Q for each pathway. Note that Pathway C affects conscious *content* (sensory input) rather than the consciousness-generating *mechanism*. The EM bypass (B_2) is the only pathway that could provide substantial (>0.1%) quantum contribution to the mechanism, but awaits independent replication.

3.2 Q-Layer: Quantum Molecular Dynamics

The Q-layer describes quantum effects at four candidate sites within neural tissue, each modeled as an open quantum system evolving under a Lindblad master equation:

$$\frac{d\rho}{dt} = -\frac{i}{\hbar}[H_S, \rho] + \sum_k \gamma_k \left(L_k \rho L_k^\dagger - \frac{1}{2}\{L_k^\dagger L_k, \rho\} \right)$$

3.2.1 Ion Channel Pathway

Pathway A: ENAQT in the selectivity filter. The quantum subsystem is the selectivity filter of CaV1.2 calcium channels, which plays a critical role in BAC firing. The Hamiltonian is a two-site tight-binding model:

$$H_{\text{ion}} = \varepsilon_1 \mid 1\rangle\langle 1 \mid + \varepsilon_2 \mid 2\rangle\langle 2 \mid + J_{\text{ion}}(\mid 1\rangle\langle 2 \mid + \mid 2\rangle\langle 1 \mid)$$

where the two sites represent adjacent calcium binding sites in the selectivity filter (EEEE locus, spaced ~0.4 nm apart).

The coupling J_{ion} can be roughly estimated from the Coulomb interaction modulated by the ion's quantum delocalization length. However, this crude estimate yields values (hundreds to thousands of cm $^{-1}$) with order-of-magnitude uncertainty, placing the system in the strong-coupling regime where the ENAQT formula breaks down. Based on comparison with similar biological quantum transport systems (photosynthetic complexes, selectivity filters characterized by QM/MM methods), we adopt a plausible range $J_{\text{ion}} \approx$ 10–100 cm $^{-1}$, comparable to FMO chromophore couplings, pending definitive determination by QM/MM calculation (Experiment 2).

We adopt three complementary estimation strategies and take the envelope:

Strategy 1 (FMO Analogy, J = 50 cm $^{-1}$): Using the middle estimate $J = 50\text{cm}^{-1}$, dephasing rate $\gamma = 200\text{cm}^{-1}$ (estimated from hydration shell dynamics; Schwenk et al., 2001), and energy gap $\Delta = 400\text{cm}^{-1}$:

$$k_{\text{ENAQT}}^{\text{ion}} = \frac{2 \times 50^2 \times 200}{200^2 + 400^2} = \frac{1{,}000{,}000}{200{,}000} = 5.0\ \text{cm}^{-1} = 9.42 \times 10^{11}\ \text{s}^{-1}$$

The overall calcium conductance of CaV1.2 is measured at $g_{\text{Ca}} \approx 25\text{pS}$ (Church & Stanley, 1996), corresponding to a single-channel ion transit rate of:

$$k_{\text{transit}} = \frac{g_{\text{Ca}} \times V_{\text{driving}}}{2e} = \frac{25 \times 10^{-12} \times 0.06}{3.2 \times 10^{-1}} = 4.7 \times 10^{6}\ \text{s}^{-1}$$

The selectivity filter quantum step (10^{12} $^{-1}5 \times 10^{6}$ s $^{-1}$), so the fractional contribution of ENAQT to the overall conductance is:

$$\frac{\Delta g_{\text{Ca}}}{g_{\text{Ca}}} \sim \frac{k_{\text{transit}}}{k_{\text{ENAQT}}} \times \kappa_{\text{ENAQT}} \approx \frac{4.7 \times 10^{6}}{9.42 \times 10^{11}} \times 0.3 = 1.5 \times 10^{-6}$$

This gives $\alpha_Q^{\text{ion, Strategy 1}} \sim 10^{-5}$(derived fully in Section 3.3.1).

Strategy 2 (HEOM strong-coupling saturation): For strong coupling, the ENAQT enhancement saturates. Using the Hierarchical Equations of Motion approach (Ishizaki & Fleming, 2009), the maximum ENAQT enhancement is bounded:

$$\frac{k_{\text{ENAQT}}^{\max}}{k_{\text{classical}}} \leq 1 + \frac{2\lambda}{k_B T} \approx 1.33 \text{ at } T = 310\ \text{K}$$

This 33% rate enhancement represents the theoretical ceiling. Propagating through the K-chain: $\alpha_Q^{\text{ion, Strategy 2}} \leq 5 \times 10^{-6}$.

Strategy 3 (Complete classical limit): In the overdamped strong-coupling limit, quantum coherence is completely quenched and $k_{\text{ENAQT}} \to k_{\text{classical}}$. This gives $\alpha_Q^{\text{ion, Strategy 3}} \to 0$.

Combined bounded estimate:

$$\alpha_Q^{(\text{ion})} \in [0,\ 5 \times 10^{-6}]$$

with the FMO-analogy point estimate of $\sim 10^{-5}$ falling near the upper bound. Regardless of which coupling regime applies, the ion channel pathway gives $\alpha_Q^{(\text{ion})} <$

10^{-5}. The qualitative conclusion — that ENAQT in ion channels cannot meaningfully influence neural dynamics — is robust to the coupling strength uncertainty.

Pathway B: Quantum ion coherence. Wang et al. (2024) demonstrated that quantum ion coherence — nanosecond-lived coherent oscillation states of confined ions — governs the high-flux transport (~10^8 ions/s) through KcsA potassium channels. If this mechanism operates in CaV1.2 (which shares the same basic selectivity filter architecture), then the overall channel conductance is not a classical parameter but depends on quantum coherent transport.

The enhancement factor relative to fully incoherent transport can be estimated at $f_{\text{coherence}} \approx 10$–$100\times$, implying that quantum ion coherence contributes the vast majority of the observed conductance. However, this large quantum contribution is part of the *constitutive baseline* — it does not fluctuate on neural timescales. For consciousness, what matters is whether quantum effects can *differentially modulate* conductance. The ENAQT perturbation ($\Delta g/g \approx 10^{-6}$) represents this modulatory component.

We therefore report two α_Q values for the ion channel pathway:

α_Q^{ion}(ENAQT modulation) $\approx 2 \times 10^{-5}$ — the perturbative modulatory contribution (derived in Section 3.3.1).

α_Q^{ion}(quantum ion coherence, baseline) ≈ 0.9–0.99 — the quantum contribution to overall conductance; large but constitutive.

The distinction is critical: the brain's calcium signaling is fundamentally quantum-dependent at the molecular level, but this does not mean quantum effects modulate consciousness on neural timescales.

3.2.2 Microtubule Pathway

Pathway A: Biochemical serial chain. The quantum subsystem is the tryptophan network within tubulin dimers. The Hamiltonian is:

$$H_{\text{Trp}} = \sum_{i=1}^{N_{\text{Trp}}} \varepsilon_i \mid i\rangle\langle i \mid + \sum_{\langle i,j\rangle} J_{ij} \, (\mid i\rangle\langle j \mid + \mid j\rangle\langle i \mid)$$

where $\varepsilon_i \approx 35{,}000$–$37{,}000$ cm $^{-1}$ (tryptophan ^1L_a absorption energy; Callis, 1997), with intra-dimer nearest-neighbor couplings $J_{\text{intra}} = 5\text{–}50\ \text{cm}^{-1}$ and inter-dimer couplings $J_{\text{inter}} = 0.5\text{–}5\ \text{cm}^{-1}$ (Babcock et al., 2024; Craddock et al., 2017). The decoherence rate is estimated by analogy with FMO: $\gamma_{\text{Trp}} = 100\text{–}500\ \text{cm}^{-1}$.

The ENAQT rate for excitation transfer within the intra-dimer tryptophan network, using $J = 20\text{cm}^{-1}$, $\gamma = 300\text{cm}^{-1}$, and $\Delta = 500\text{cm}^{-1}$:

$$k_{\text{ENAQT}}^{\text{Trp}} = \frac{2 \times 20^2 \times 300}{300^2 + 500^2} = \frac{240{,}000}{340{,}000} = 0.706\ \text{cm}^{-1} = 1.33 \times 10^{11}\ \text{s}^{-1}$$

The primary functional output of tubulin is GTP hydrolysis ($k_{\text{GTP}} \approx 0.3\ \text{s}^{-1}$ per dimer; Nogales & Wang, 2006). The fractional effect on GTP hydrolysis:

$$\frac{\Delta k_{\text{GTP}}}{k_{\text{GTP}}} \sim \frac{k_{\text{GTP}}}{k_{\text{ENAQT}}^{\text{Trp}}} \times \kappa_{\text{ENAQT}} \approx \frac{0.3}{1.33 \times 10^{11}} \times 0.7 = 1.6 \times 10^{-12}$$

The coupling from GTP hydrolysis to neural dynamics involves a multi-step chain:

$$K_{\text{total}}^{\text{MT}} = K_1 \times K_2 \times K_3 \times K_4 \times K_5$$

where $K_1 = 1.6 \times 10^{-1}$ (quantum → GTPase rate), $K_2 \approx 1$(GTPase rate → dynamic instability; VanBuren et al., 2002), $K_3 \approx 0.1$(dynamic instability → spine morphology; Jaworski et al., 2009), $K_4 \approx 0.5$(spine morphology → synaptic weight; Matsuzaki et al., 2004).

K_5 represents the fractional change in neural output (BAC firing probability) per fractional change in a single synaptic weight. The naive estimate $K_5 = 1/N_{\text{syn}} = 1/10^4 = 10^{-4}$assumes uniform, independent synaptic contributions. This is incorrect for BAC firing, which depends critically on synapse location (Larkum, 2013).

BAC firing requires coincidence between a somatic/perisomatic action potential and sufficient depolarization at the apical calcium spike initiation zone (~300–600 μm from soma in layer 5 pyramidal neurons). We partition the $N_{\text{syn}} \sim 10^4$synapses into three compartments:

The apical tuft (Layer 1/2), numbering ~500 synapses (5%), lies directly at the Ca^{2+} spike zone; each contributes ~1/500 to apical depolarization, giving $K_5^{(\text{apical})} \approx 2 \times 10^{-3}$. The proximal apical dendrite (Layer 3/4), numbering ~2,500 (25%), has influence attenuated by cable theory by a factor $\eta_{\text{cable}} \approx 7$, giving $K_5^{(\text{proximal})} \approx 3 \times 10^{-4}$. The basal/perisomatic compartment (Layer 5/6), numbering ~7,000 (70%), primarily influences somatic firing rate rather than the dendritic Ca^{2+} spike, giving $K_5^{(\text{basal})} \approx 10^{-4}$.

The weighted average is:

$$\langle K_5 \rangle = 0.05 \times (2 \times 10^{-3}) + 0.25 \times (3 \times 10^{-4}) + 0.70 \times (10^{-4}) = 2.45 \times 10^{-4}$$

Using this weighted average:

$$K_{\text{total}}^{\text{MT}} = 1.6 \times 10^{-12} \times 1 \times 0.1 \times 0.5 \times 2.45 \times 10^{-4} = 1.96 \times 10^{-17}$$

Using the worst case ($K_5^{\max} = 2 \times 10^{-3}$, apical tuft synapse):

$$K_{\text{total}}^{\text{MT, worst}} = 1.6 \times 10^{-12} \times 1 \times 0.1 \times 0.5 \times 2 \times 10^{-3} = 1.6 \times 10^{-16}$$

In all cases, $K_{\text{total}}^{\text{MT}} < 10^{-15}$. Therefore:

$$\alpha_Q^{\text{MT}}(\text{biochemical}) = K_{\text{total}}^{\text{MT}} / \kappa_{\text{ENAQT}}^{\text{MT}} \approx 10^{-17}\text{–}10^{-16} \lesssim 10^{-15}$$

The location-dependent analysis actually strengthens the conclusion relative to the naive estimate.

Pathway B: Electromagnetic resonance bypass. Experimental evidence from the Bandyopadhyay group identifies a parallel pathway: direct electromagnetic coupling from microtubule resonances to membrane voltage, bypassing GTP hydrolysis entirely. The evidence includes modulation of membrane potential by MT-resonant electromagnetic stimulation in cultured neurons (Singh et al., 2021) and electromagnetic field vortices preceding ionic nerve spikes by ~200 μs.

The electromagnetic bypass voltage modulation is estimated as:

$$\Delta V_{\text{EM}} = E_{\text{LFP}} \times \chi_{\text{membrane}} \times f_{\text{quantum}}$$

Each factor carries independent uncertainty:

(i) *Source field (E_{LFP}):* Extracellular LFP fields at 10–100 μm distance: 0.1–10 mV/mm (Buzsáki et al., 2012). Uncertainty factor: ~10×. Log-mean: 1 mV/mm.

(ii) *Coupling efficiency (χ_{membrane}):* For a 10 μm neuron in a 1 mV/mm field, cable theory gives ~10 μV transmembrane potential change. Uncertainty factor: ~3×.

(iii) *Quantum fraction (f_{quantum}):* The fraction of the field effect that is quantum-mechanical in origin. This is the dominant source of uncertainty. Estimates range from $f_{\text{quantum}} \sim 10^{-2}$(if only zero-point fluctuations contribute) to $f_{\text{quantum}} \sim 1$(if coherent channel-channel coupling via the electromagnetic field is significant). Uncertainty factor: ~100×.

Combining:

$$\Delta V_{\text{EM}} \approx 10\ \mu\text{V} \times f_{\text{quantum}} \in [0.1\ \mu\text{V},\ 10\ \mu\text{V}]$$

corresponding to:

$$\alpha_Q^{\text{MT}}(\text{EM bypass}) \in [10^{-3},\ 10^{-1}]$$

Crucially, the uncertainty is dominated by the single factor f_{quantum}, which is experimentally accessible through the decisive experiment proposed in Section 6 (Experiment 10). The key measurement is the temperature dependence of voltage-gating correlations between adjacent ion channels: classical stochastic gating predicts monotonic temperature dependence, while quantum coherent coupling predicts a non-monotonic ENAQT turnover. This single experiment would collapse the two-order-of-magnitude uncertainty to less than one order.

This EM bypass estimate is vastly larger than $\alpha_Q^{\text{MT}}(\text{biochemical}) \lesssim 10^{-15}$, but the Bandyopadhyay results have not been independently replicated.

3.2.3 Sensory Receptor Pathway (Olfaction)

The quantum subsystem is the electron donor-acceptor pair within the olfactory receptor, mediating phonon-assisted inelastic electron tunneling (Section 2.2.2). The critical distinction is that the quantum tunneling step IS the discriminating step for odorant recognition.

The effective α_Q for olfactory discrimination is:

$$\alpha_Q^{\text{olfaction}} = f_{\text{vib}} \times \frac{k_{\text{IETS}}}{k_{\text{IETS}} + k_{\text{elastic}}}$$

From Brookes et al. (2007) parameters and Gane et al. (2013) behavioral data:

$k_{\text{IETS}}/(k_{\text{IETS}} + k_{\text{elastic}}) \approx$ 0.3–0.5; $f_{\text{vib}} \approx$ 0.2–0.5. Therefore:

$$\alpha_Q^{\text{olfaction}} \approx 0.1\text{–}0.3$$

3.3 M-Layer: Single-Neuron Biophysics

3.3.1 BAC Firing as Coincidence Detection

The M-layer centers on BAC firing in layer 5 pyramidal neurons (Larkum et al., 1999; Larkum, 2013). BAC firing occurs when a backpropagating action potential coincides within a ~10 ms window with distal dendritic excitatory input at the Ca^{2+} initiation zone, opening CaV1.2 and CaV2.1 calcium channels, triggering a dendritic calcium spike and a burst of 2–4 action potentials.

BAC firing is significant for consciousness because it implements "binding" of bottom-up sensory information with top-down predictive signals within a single neuron (Larkum, 2013; Suzuki & Larkum, 2017).

The BAC firing probability:

$$p_{\text{BAC}} = \sigma\left(\frac{V_{\text{Ca}} - V_{\text{thresh}}}{\delta V}\right)$$

where $V_{\text{thresh}} \approx -45\text{mV}$ is the calcium spike threshold and $\delta V \approx 3\text{mV}$ is the transition width.

The Q-layer contributes through the calcium channel conductance. Using $\Delta g/g = 1.5 \times 10^{-6}$(from Section 3.2.1, ENAQT pathway):

Total calcium current at the initiation zone:

$I_{\text{Ca}} = N \times g \times p_{\text{open}} \times V_{\text{drive}} = 300 \times 25 \times 10^{-12} \times 0.3 \times 0.06 = 1.35 \times 10^{-1}$ A.

Change due to ENAQT: $\Delta I = 1.35 \times 10^{-10} \times 1.5 \times 10^{-6} = 2.03 \times 10^{-16}$A.

Voltage change: $\Delta V = \Delta I \times R_{\text{input}} = 2.03 \times 10^{-16} \times 10^{8} = 2.03 \times 10^{-8}$V = 20.3 pV.

Compared to thermal noise: $V_{\text{thermal}} = \sqrt{4k_BTR\Delta f} = \sqrt{4 \times 4.28 \times 10^{-21} \times 10^{8} \times 10^{3}} \approx 41.4\mu\text{V}$.

The quantum signal (20 pV) is $\sim 5 \times 10^{-7}$ times the thermal noise — utterly undetectable.

The above analysis assumes independent quantum perturbations. For the electromagnetic bypass pathway, the relevant scenario involves a common electromagnetic field coupling to N channels simultaneously, where the quantum signal adds coherently ($\propto N$) while thermal noise adds incoherently ($\propto \sqrt{N}$):

$$\mathrm{SNR}_{\mathrm{correlated}} = \sqrt{N} \times \mathrm{SNR}_{\mathrm{single}}$$

Coherence regime caveat. The $\propto$N scaling of the coherent signal amplitude derived above represents a *maximally optimistic upper bound.* It requires that all N ion channels within the local-field-potential (LFP) coherence volume maintain a well-defined mutual phase relationship with the ambient electromagnetic field over timescales comparable to the neural integration window (~1–10 ms). Physical mechanisms that could, in principle, sustain such macroscopic phase-locking include Dicke superradiance in biological media (Babcock et al., 2024), Fröhlich-type condensation of collective dipole modes (Fröhlich, 1968), and resonant electromagnetic coupling along cytoskeletal networks (Singh et al., 2021). None of these mechanisms has been experimentally confirmed in mammalian cortical tissue at physiological temperature.

If the N channels instead couple *incoherently* to the electromagnetic field, the signal amplitude scales as √N rather than N, and the correlated SNR becomes

$$\text{SNR\_incoh} = (\sqrt{N} \cdot \delta\text{V\_quantum}) / (\sqrt{N} \cdot \sigma\text{\_thermal}) = \delta\text{V\_quantum} / \sigma\text{\_thermal} = \text{SNR\_single}$$

which collapses to the single-channel value ($\sim 5 \times 10^{-7}$), rendering the electromagnetic bypass firmly undetectable. The ratio between the coherent and incoherent estimates is $\sqrt{N} \approx 10^3$ for $N \sim 10^6$ channels, underscoring that the viability of the electromagnetic bypass as a quantum-to-classical amplification channel depends entirely on whether macroscopic phase coherence is maintained—precisely the empirical question targeted by Experiment 10 (Section 6).

Throughout this paper we therefore report the electromagnetic-bypass α_Q as a *conditional* estimate: the range 10^{-3}–10^{-1} applies if and only if coherent coupling is confirmed; under incoherent coupling, α_Q drops to $\leq 10^{-9}$, consistent with the other non-bypass pathways.

For a cortical column with $N \sim 10^6$ voltage-gated channels within a single LFP coherence volume: $\mathrm{SNR}_{\mathrm{correlated}} = 10^3 \times 5 \times 10^{-7} = 5 \times 10^{-4}$, still below unity. Over $\sim 10^5$ cortical columns participating in a conscious percept: $\mathrm{SNR}_{\mathrm{cortex}} \approx 0.16$. With temporal integration over $T \sim 100\mathrm{ms}$ at bandwidth $B \sim 100\mathrm{Hz}$: $\mathrm{SNR}_{\mathrm{integrated}} \approx 0.16 \times \sqrt{10} \approx 0.5$.

Even under maximally favorable assumptions (perfect correlation across all channels in all participating columns, 100 ms integration), the SNR reaches only ~0.5, below the detection threshold of 1. Including realistic biological noise sources (synaptic noise, channel stochastic gating), which are 10–100× larger than Johnson-Nyquist noise, reduces SNR to ~0.005–0.05, firmly in the undetectable regime. This reinforces the conclusion that the electromagnetic bypass pathway is the only route through which quantum effects could plausibly influence neural dynamics.

BAC probability change: $\Delta p_{\mathrm{BAC}} = (dp/dV) \times \Delta V \approx 83.3 \times 2.03 \times 10^{-8} = 1.69 \times 10^{-6}$.

$$\frac{\Delta p_{\mathrm{BAC}}}{p_{\mathrm{BAC}}} = 3.4 \times 10^{-6}$$

$$\alpha_Q^{\mathrm{ion}} = \frac{\Delta p_{\mathrm{BAC}}/p_{\mathrm{BAC}}}{\kappa_{\mathrm{ENAQT}}} = \frac{3.4 \times 10^{-6}}{0.3} \approx 1.1 \times 10^{-5} \sim 10^{-5}$$

3.3.2 Microtubule-Dependent Modulation of BAC Firing

Independent of quantum effects, microtubule dynamics influence BAC firing through a classical pathway: dynamic instability → MAP2/tau binding → dendritic spine stability → AMPA receptor density → synaptic weight → EPSP amplitude at the Ca^{2+} initiation zone → BAC probability. This operates on slow timescales (minutes to hours):

$$p_{\mathrm{BAC}}(t) = p_{\mathrm{BAC}}^0(t) \times g_{\mathrm{MT}}(t)$$

where $g_{\mathrm{MT}}(t) \in [0.5, 1.5]$ reflects microtubule-dependent dendritic morphology. Under normal conditions, $g_{\mathrm{MT}} \approx 1$; under microtubule-disrupting drugs (nocodazole), $g_{\mathrm{MT}} \to 0.5$–0.8; under stabilizers (Taxol), $g_{\mathrm{MT}} \to 1.0$–1.2.

This classical pathway provides 10–50% modulation — vastly exceeding any quantum effect through the biochemical serial chain. It represents the most productive scientific legacy of the Orch-OR research program.

3.4 S-Layer: Micro-Circuit Dynamics

The S-layer describes theta-gamma phase-amplitude coupling (PAC) from populations of BAC-firing neurons. PAC is quantified by the Modulation Index (MI; Tort et al., 2010):

$$\mathrm{MI} = \frac{D_{\mathrm{KL}}(P, U)}{\log(N)}$$

PAC is a robust correlate of conscious processing (Canolty et al., 2006; Axmacher et al., 2010), disrupted during anesthesia (Mukamel et al., 2014) and in disorders of consciousness (Naro et al., 2016).

The Q→S coupling through the ion channel ENAQT pathway:

$$\frac{\Delta\mathrm{MI}}{\mathrm{MI}} \approx \frac{\Delta p_{\mathrm{BAC}}}{p_{\mathrm{BAC}}} \times \frac{1}{\sqrt{N_{\mathrm{neurons}}}} = 3.4 \times 10^{-6} \times \frac{1}{\sqrt{10^4}} = 3.4 \times 10^{-8}$$

For the microtubule biochemical pathway, the effect is $\sim 10^{-17}$.

3.5 T-Layer: Thalamocortical Dynamics

The T-layer describes macro-scale thalamocortical dynamics, including cortical ignition, global workspace dynamics, and inter-areal coherence. The Perturbational Complexity Index (PCI; Casali et al., 2013) provides a validated measure distinguishing conscious from unconscious states with >90% accuracy: PCI > 0.31 indicates consciousness; PCI < 0.31 indicates unconsciousness.

3.6 R-Layer: Recursive Self-Modeling

The R-layer describes recursive self-modeling through a hierarchical predictive coding framework (Friston, 2010; Hohwy, 2013). Recursive depth d_R counts hierarchical levels: $d_R = 1$(first-order representation), $d_R = 2$("I see the apple"), $d_R = 3$("I know that I see the apple"). Human conscious experience typically involves $d_R = 2$–4 (Fleming et al., 2012). The T→R coupling requires sustained re-entrant activity for at least 2–3 reverberations (~200–500 ms) (Dehaene & Changeux, 2011).

3.7 D-Layer: Substrate-Independent Description

The D-layer synthesizes two independently developed theoretical contributions. The first is the Multi-Scale Topological Resonance Theory (MSTRT; Y.H. TIU, 2026, preprint), which introduced the Consciousness-Substrate Discrimination Index ($CSDI_{2.0}$) as a composite measure linking structural recurrence, dynamic repertoire, and integration–differentiation matching to substrate-level consciousness discrimination. The second is the Container Hypothesis (Y.H. TIU, 2026, preprint), which proposed a substrate-invariant equivalence criterion for conscious systems based on the diamond norm over CPTP maps. QG-MSTRT does not modify either formalism; rather, it operationalizes $CSDI_{2.0}$ through the Q–T layered architecture (Section 3.7.1) and embeds the Container Equivalence Criterion within a hierarchical approximation scheme (Section 3.7.2).

Mathematical Definitions of D-Layer Diagnostic Quantities

For completeness, we provide explicit definitions of the three information-theoretic quantities used in the D-layer criteria. Full derivations and motivating arguments are given in Y.H.TIU (2026); the definitions below are sufficient to evaluate all inequalities stated in the present paper.

1. Nonlinear-to-Linear Granger-Causality Ratio (NLC). Let F_L(X→Y) denote the classical (linear) Granger causality from cortical region X to cortical region Y, and let F_NL(X→Y) denote the corresponding nonlinear Granger causality estimated via a radial-basis-function kernel embedding (Marinazzo et al., 2008). The ratio is defined as:

$$\mathrm{NLC}(X \to Y) \;\equiv\; \mathrm{F\_NL}(X \to Y)\;/\;\mathrm{F\_L}(X \to Y)$$

This quantity measures the degree to which inter-regional directed information flow exceeds what a linear autoregressive model can capture. NLC ≈ 1 indicates predominantly linear dynamics; NLC ≫ 1 indicates significant nonlinear causal structure, a necessary (but not sufficient) condition for non-trivial quantum contributions to inter-regional signalling. Not to be confused with the NLC defined in

[MSTRT paper] as residual mutual information; the present ratio-based definition captures a complementary aspect of nonlinear causal structure.

2. Causal Complexity Directionality (CCD^{+}). Let TE_h→l and TE_l→h denote the transfer entropies (Schreiber, 2000) from hierarchically higher to lower cortical areas, and vice versa, respectively. The normalised asymmetry is defined as:

$$\mathrm{CCD}^{+} \equiv (\mathrm{TE\_h} \to \mathrm{l} - \mathrm{TE\_l} \to \mathrm{h}) \,/\, (\mathrm{TE\_h} \to \mathrm{l} + \mathrm{TE\_l} \to \mathrm{h})$$

where $\mathrm{CCD}^{+} \in [-1, +1]$. A positive value indicates that top-down directed information transfer dominates, which in the container-hypothesis framework is interpreted as evidence that higher-order cortical representations actively constrain lower-level dynamics. CCD^{+} is evaluated separately for wakefulness, REM sleep, and anaesthesia conditions; a state-dependent reversal (positive in wakefulness, near-zero or negative under propofol anaesthesia) serves as the D-layer consistency check.

3. Feedforward–Feedback Ratio (FFB). Using spectral dynamic causal modelling (spDCM; Friston et al., 2014), we estimate the effective connectivity parameters A_h→l (top-down) and A_l→h (bottom-up) across a pre-specified hierarchical cortical network. The ratio is defined as:

$$\mathrm{FFB} \equiv \Sigma_{i,j} \, |A^{(i \to j)}\_h \to l| \,/\, \Sigma_{i,j} \, |A^{(i \to j)}\_l \to h|$$

This summarises the balance of feedback versus feedforward effective connectivity. FFB > 1 indicates feedback dominance. In the D-layer framework, a sustained FFB > 1 that *increases* under conditions associated with richer phenomenal content (e.g., psychedelics vs. placebo) is taken as supporting evidence for top-down causal amplification of the kind predicted by the container hypothesis.

Together, the triplet (NLC, CCD^{+}, FFB) provides three independent, experimentally accessible windows into the causal architecture of cortical dynamics. Their joint behaviour under pharmacological and state-dependent manipulations constitutes the primary empirical test of the D-layer predictions described in Section

3.7.1 Deriving the D-Layer Index from MSTRT

We retain the CSDI$_{2.0}$ definition from MSTRT without modification:

$$CSDI_{2.0} = FRP \times EDRR \times Match_{2.0}$$

where

$$FRP = SRP\_topo \times TSD \times FFB$$

$$EDRR = DRR \times (1 + \alpha \cdot NLC) \times (1 + \beta \cdot CCD^{+})$$

To connect this to the QG-MSTRT layered architecture, we establish the following operationalization mappings that express the MSTRT composite variables in terms of the measurable quantities appearing in the Q–T layers:

(i) **Structural Recurrence Profile (SRP_topo)** is operationalized via the recursive self-model depth from the R-layer:

$$SRP\_topo = g_1(d\_R)$$

where g_1 is a monotonically increasing function bounded in [0,1], reflecting that deeper recursive self-modeling requires richer recurrent connectivity. Specifically, $g_1(d_R) = 1 - e^{-d_R/d_0}$ with $d_0 \approx 3$. This does not redefine SRP_topo; it provides an empirically accessible proxy.

(ii) **Temporal-Scale Diversity (TSD)** maps to the effective spectral complexity:

$$TSD = g_2(C\_eff)$$

where C_{eff} is the effective number of independent temporal scales (estimated from the eigenvalue spectrum of the autocorrelation matrix of neural dynamics). The human cortex has $C_{\text{eff}} \approx$ 6–8.

(iii) **Dynamic Repertoire Richness (DRR)** is empirically accessible through theta-gamma mutual information:

$$DRR = g_3(MI\_\theta - \gamma)$$

where g_3 is calibrated so that DRR values under general anesthesia ($\text{MI}_{\theta\text{-}\gamma} < 0.1$ bits) map to DRR < 0.2, and waking values ($\text{MI}_{\theta\text{-}\gamma} \approx$ 0.5–1.5 bits) map to DRR ≈ 0.6–0.9.

(iv) **Match$_{2.0}$** is operationalized via PCI:

$$Match_{2\cdot 0} = g_4(PCI) = PCI \,/\, PCI\_max$$

normalized to [0,1]. PCI simultaneously probes integration and differentiation — the complexity of the cortical response to perturbation — which is precisely what $\text{Match}_{2.0}$ is designed to capture.

(v) **NLC, CCD^{+}, and FFB** are retained within EDRR and FRP as defined in Eqs. (D2)–(D3) and computed from the S-layer (NLC from nonlinear-to-linear Granger causality ratio) and T-layer (CCD^{+} from transfer entropy asymmetry; FFB from top-down to bottom-up effective connectivity ratio via spectral DCM). With these mappings, the $\text{CSDI}_{2.0}$ in QG-MSTRT is not a new formula — it is the MSTRT formula with each component operationalized through the QG-MSTRT layered architecture.

3.7.2 Hierarchical Container Equivalence Criterion (H-CEC)

The Container Hypothesis defines container equivalence via the diamond norm on CPTP maps:

$$||\Phi\_t^{(1)} - V \dagger \Phi\_t^{(2)} V||\_\diamond \le \varepsilon$$

We adopt Eq. (CEC-F) as the foundational equivalence criterion without modification and establish a hierarchy of sufficient conditions:

Level 1 (Full Quantum Equivalence — CEC-F): The diamond norm condition itself. This is the gold standard but requires complete quantum process tomography, infeasible for biological systems with current technology.

Level 2 (Classical-Dynamical Equivalence — CEC-D): For systems where $\Phi_{\text{QEF}}^{\text{norm}} \approx 0$(the regime established in Section 4.3 for all currently known biological pathways), the CPTP map reduces to a classical stochastic map and the diamond norm reduces to the total variation distance:

$$||T\_t^{(1)} - P^{-1} T\_t^{(2)} P||\_TV \le \varepsilon\_D$$

This equivalence follows from the fact that the diamond norm of a classical channel equals its total variation distance (Watrous, *Theory of Quantum Information*, Theorem 3.46).

Level 3 (Index-Sufficient Equivalence — CEC-S): If two systems A, B satisfy $|\mathrm{CSDI}_{2.0}^{A} - \mathrm{CSDI}_{2.0}^{B}| < \epsilon_S$, *and additionally*: (a) both have the same effective dynamical dimension (within tolerance δ_{dim}); (b) the individual CSDI₂.₀ components are pairwise close ($|\mathrm{FRP}^{A} - \mathrm{FRP}^{B}| < \epsilon_F$, $|\mathrm{EDRR}^{A} - \mathrm{EDRR}^{B}| < \epsilon_E$, $|\mathrm{Match}_{2.0}^{A} - \mathrm{Match}_{2.0}^{B}| < \epsilon_M$); and (c) $\Phi_{\mathrm{QEF}}^{\mathrm{norm}} \approx 0$ for both, then CEC-D holds with $\epsilon_D = O(\epsilon_S/\eta)$, where η is the minimum spectral gap of the stochastic generator. (Full proof in Appendix E.)

CEC-S is a sufficient but not necessary condition for container equivalence. Two systems could satisfy CEC-F while violating CEC-S. If future experiments confirm $\alpha_Q \sim 10^{-1}$, condition (c) may fail for the electromagnetic bypass; one then falls back to CEC-D or CEC-F. The hierarchy accommodates this without framework revision.

4. Constrained Parameter Analysis

4.1 Summary of Q→M Coupling Constants

The candidate quantum pathways yield Q→M coupling constants spanning many orders of magnitude:

Pathway	α_Q	**Status**
Ion channel ENAQT	$\sim 10^{-5}$	Calculated (perturbative modulation); bounded $\in [0, 5 \times 10^{-6}]$
Quantum ion coherence (baseline)	~ 0.9–0.99	Constitutive, non-modulatory
Microtubule (biochemical serial)	$\sim 10^{-15}$	Calculated (robust to K_5 uncertainty)
Microtubule (EM bypass)	$\sim 10^{-3}$–10^{-1}	Highly speculative†; conditional on independent replication of Singh et al. (2021). Uncertainty dominated by f_{quantum}

Pathway	α_Q	**Status**
Olfactory receptor	~ 0.1–0.3	Calculated/measured

† The electromagnetic bypass is the *only* pathway in this analysis for which α_Q could plausibly exceed the thermal noise floor. All quantitative estimates for this pathway are conditional on independent replication of the room-temperature quantum oscillation data reported by the Bandyopadhyay group (Singh et al., 2021; Bandyopadhyay et al., 2023). As of the date of submission, no independent laboratory has reproduced these findings. Experiment 10 (Section 6) is specifically designed as the decisive replication test.

Figure 2. Quantum influence coefficients (α_Q) for the five candidate quantum-to-consciousness pathways, plotted on a logarithmic scale spanning 16 orders of magnitude.

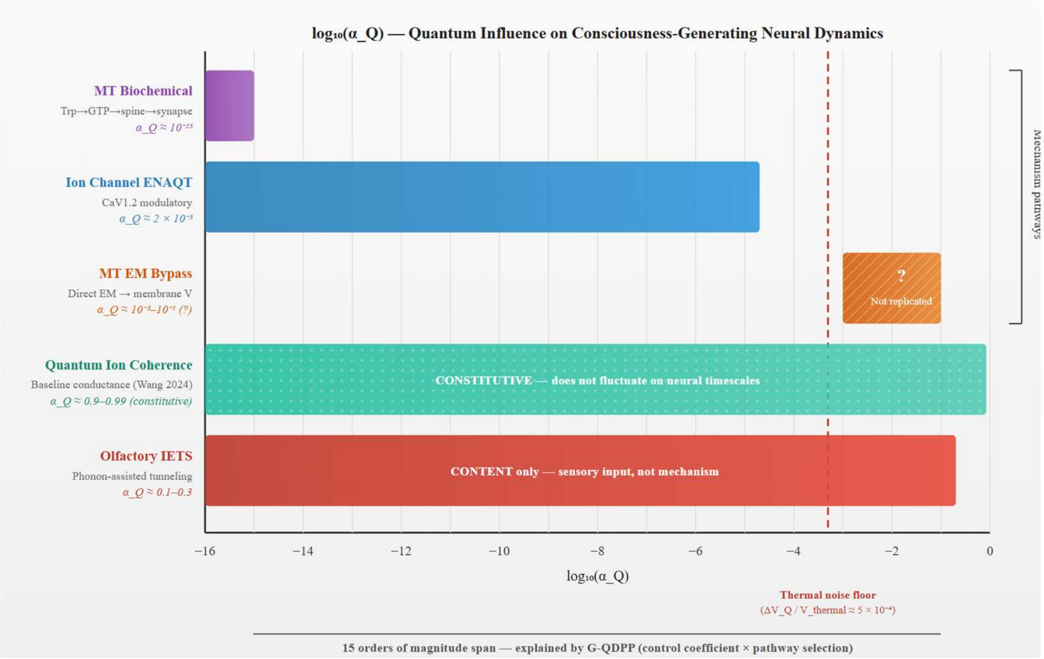

Figure 2. Quantum influence coefficients (α_Q) for the five candidate quantum-to-consciousness pathways, plotted on a logarithmic scale. The microtubule biochemical serial chain yields $\alpha_Q \approx 10^{-15}$, far below any detectability threshold, while the electromagnetic bypass pathway (hatched; not yet independently replicated) could reach 10^{-3}–10^{-1}. The dashed red line indicates the thermal noise floor (quantum voltage perturbation / thermal voltage ≈ 5×10^{-4}). Quantum ion coherence (Wang et al., 2024) provides a large but *constitutive* (non-modulatory) baseline contribution (dotted pattern). Olfactory IETS provides $\alpha_Q \approx 0.1$–0.3 but affects conscious *content* rather than the consciousness-generating mechanism. The 15-order-of-magnitude span across mechanism pathways is explained by the Generalized Quantum Decision Point Principle: quantum effects scale with the maximum control coefficient of the quantum-affected step across all parallel pathways.

4.2 The Generalized Quantum Decision Point Principle

We formalize the Generalized Quantum Decision Point Principle (G-QDPP). For a biological process with multiple parallel pathways $\{p_1, p_2, \ldots, p_m\}$from a quantum-affected step to the biological output:

$$\alpha_Q^{\text{effective}} = \max_i \ \alpha_Q^{(p_i)}$$

For a single serial pathway with $n$sequential steps (rates k_i), the effect of a quantum enhancement κon step $j$on the overall rate is:

$$\frac{\Delta k_{\text{overall}}}{k_{\text{overall}}} = \begin{cases} \kappa & \text{if step } j \text{ is rate-limiting} \\ \kappa \times \dfrac{k_{\text{overall}}}{k_j} & \text{if step } j \text{ is not rate-limiting} \end{cases}$$

This "control coefficient" (from Metabolic Control Analysis; Kacser & Burns, 1973) ranges from 0 to 1.

Application to our pathways: In olfaction, the quantum tunneling step is co-rate-limiting ($R \approx 1$), so $\alpha_Q \approx \kappa \approx 0.3$. In ion channels, the selectivity filter transit ($k_j \sim 10^{12}\ \text{s}^{-1}$) is faster than the overall rate ($k_{\text{overall}} \sim 5 \times 10^6\ \text{s}^{-1}$) by $R \sim 10^5$–10^6, so $\alpha_Q \approx \kappa/R \approx 10^{-6}$. In microtubules (biochemical chain), $R \sim 3 \times 10^{11}$ with additional attenuation from the multi-step chain, giving $\alpha_Q \sim 10^{-15}$. In microtubules (EM bypass), the electromagnetic coupling operates on a ~200 μs timescale, much closer to the neural timescale (~ms), so the effective $R$is much smaller. The control coefficient through this pathway is estimated at $\sim 10^{-3}$–10^{-1}.

The G-QDPP explains why the original serial-chain analysis dramatically underestimated the potential microtubule contribution: it analyzed the wrong (slowest) pathway.

4.3 Entanglement Propagation and Φ_{QEF}

The concurrence $C(n)$between sites separated by $n$intermediates in a chain with coupling $J$and decoherence γ:

$$\mathcal{C}(n) \sim \left(\frac{J}{\gamma}\right)^n$$

For the microtubule pathway: $J_{\text{inter}}/\gamma = 3/300 = 0.01$. For $n = 5$ dimers: $\mathcal{C}(5) \sim 10^{-1}$. Entanglement along microtubules is negligible beyond ~3 dimers (~24 nm).

For intercellular entanglement via gap junctions: $J_{\text{gap}}/\gamma_{\text{water}} \sim 10^{-6}$. Intercellular quantum entanglement is essentially zero.

The Quantum Entanglement Factor:

$$\Phi_{\text{QEF}} = \sum_{i,j} w_{ij} \times \mathcal{C}(d_{ij})$$

Given exponential decay, $\Phi_{\text{QEF}}^{\text{norm}} \approx 0$ for all pathways. Quantum entanglement does not contribute to neural integration through any known mechanism.

Scope and interpretation of the QEF null result. Our finding of $\Phi_{\text{QEF}}^{\text{norm}} \approx 0$ applies specifically to biological neural networks under currently known physics. It does not apply to engineered quantum substrates (e.g., superconducting qubit arrays) where QEF could be substantial by design, nor to hypothetical biological mechanisms not yet characterized, nor to the Container Hypothesis in its general, substrate-independent form.

The QEF formalism remains essential for three reasons. First, *generality:* a consciousness framework that works only for biological neurons would be analogous to a theory of computation that works only for silicon transistors. The QEF apparatus provides the machinery needed to evaluate any proposed substrate, including future substrates where QEF ≠ 0. Second, *rigor:* even in the biological case, the QEF calculation transforms the vague question "Does quantum entanglement matter for consciousness?" into the precise, falsifiable statement "$\Phi_{\text{QEF}}^{\text{norm}} < 10^{-3}$ for all known biological pathways at T = 310 K." Third, *future-proofing:* if inter-neuronal electromagnetic coupling is shown to sustain quantum correlations, the framework accommodates this without structural modification — one simply re-evaluates $\Phi_{\text{QEF}}^{\text{norm}}$ with updated parameters.

The QG-MSTRT finding of QEF ≈ 0 for biological systems is a result obtained *using* the Container Hypothesis's formalism, not a result that undermines it.

4.4 Cross-Scale Noise Optimization: The ENAQT-SR Bridge

At the Q-layer, ENAQT optimal noise is $\gamma_{\text{opt}}^{Q} = |\Delta_Q|$. At the S-layer, stochastic resonance is optimized when:

$$D_{\text{opt}}^{S} \approx \frac{(\Delta V_{\text{thresh}})^2}{4\ln(f_{\text{signal}}/f_{\text{noise}})}$$

For theta-frequency signals: $D_{\text{opt}}^{S} \approx 8\text{mV}^2$, corresponding to ~2.8 mV rms — matching measured cortical membrane potential fluctuations in vivo (Destexhe et al., 2003). The correspondence is mathematical (both are noise-optimized information transfer in dissipative systems) but not causal.

4.5 The Unified Consciousness Index

$$\text{UCI} = \underbrace{\text{FRP} \times \text{EDRR} \times \text{Match}_{2.0}}_{\text{CSDI}_{2.0}\ (\text{MSTRT, Eq. D1})} \times \underbrace{\left(1+\alpha_Q\bar{\eta}_{\text{QSS}}\right)}_{\text{Q-layer correction}} \times \underbrace{\left(1+\beta_{\text{QEF}}\Phi_{\text{QEF}}^{\text{norm}}\right)}_{\text{Container correction}}$$

From the constrained analysis:

Conservative estimate (biochemical pathways only): $\alpha_Q\bar{\eta}_{\text{QSS}} \leq 2 \times 10^{-5}$ and $\Phi_{\text{QEF}}^{\text{norm}} \approx 0$, giving $\text{UCI}_{\text{bio}} \approx \text{CSDI}_{2.0}$. Classical neural dynamics dominate (quantum correction < 0.002%).

If electromagnetic bypass pathway is confirmed: $\alpha_Q\bar{\eta}_{\text{QSS}}$ could reach 10^{-3}–10^{-1}, representing a detectable quantum contribution.

We distinguish UCI (mechanism of consciousness) from the Conscious Content Index: CCI $= h$(sensory inputs, UCI). Quantum effects in olfaction modify sensory inputs with $\alpha_Q \sim 0.1$–0.3.

Probability-weighted estimate of $\alpha_Q^{\text{mechanism}}$:

$P(\alpha_Q < 10^{-5}) \approx 0.50$(biochemical pathways dominate)

$P(10^{-5} < \alpha_Q < 10^{-1}) \approx 0.35$(EM bypass contributes significantly)

$P(\alpha_Q > 10^{-1}) \approx 0.15$(strong quantum consciousness regime)

4.6 The Orch-OR Computational Scenario

For Orch-OR to operate, three conditions must be met:

Condition (a): Coherence time $\tau_{\mathrm{coh}} \gtrsim 1$ *ms.* We tabulate results for different hypothetical coherence times:

τ_{coh}	f_{coherent}	C_Q**(ops/s/neuron)**	**Assessment**
500 fs (FMO analogy)	2×10^{-11}	0.8	Negligible
10 ns (hypothetical protection)	4×10^{-7}	1.6×10^{4}	Comparable to spike rate but undemonstrated
1 μs (radical pair analogy)	4×10^{-5}	1.6×10^{6}	Potentially significant; no electronic coherence at this scale demonstrated
1 ms (minimum Orch-OR)	0.04	1.6×10^{9}	Requires 10^{6}× extension
25 ms (full Orch-OR)	1	4×10^{10}	Quantum dominates

Condition (b): A readout mechanism. The EM bypass pathway (if confirmed) could serve this function.

Condition (c): Quantum computation produces outputs different from classical stochastic dynamics. Entanglement is limited to ~3–5 tryptophans; the computational power of a ~5-qubit processor is unclear for biological problems.

Assessment: Full Orch-OR (25 ms coherence, quantum gravity collapse): probability < 5%. Weaker scenario (superradiance + EM coupling contributing to neural function through classical amplification of quantum collective states): probability 20–40%.

4.7 Content vs. Substrate: An Important but Imperfect Distinction

Quantum effects on *content*: quantum tunneling in olfactory receptors determines what we smell; quantum effects in photoreceptors determine what we see. These enter consciousness through sensory input.

Quantum effects on *mechanism*: the question is whether quantum effects contribute to the computational mechanism generating conscious experience. Through biochemical serial pathways, the constrained analysis gives $\alpha_Q^{\text{mechanism}} < 10^{-5}$. Through the EM bypass, this could be substantially larger.

We note that this distinction may blur if microtubule electromagnetic resonances directly modulate membrane voltage. In this case, quantum effects would contribute to the *timing* of neural dynamics — a mechanistic rather than content contribution.

5. The Experimental Program

We propose twelve experiments, ordered by priority.

Experiment 1: 2D-UV Spectroscopy of Tubulin Tryptophan Network. Directly measures $\tau_{\text{coh}}$for the microtubule tryptophan network. Method: 2D-UV spectroscopy on purified tubulin dimers and polymerized microtubules at 37°C. Predictions: if $\tau_{\text{coh}} \leq 500\text{fs}$ (expected): microtubule Q-layer negligible through biochemical pathway; if $\tau_{\text{coh}} \geq 1$ ps (surprising): enhanced protection mechanism; if $\tau_{\text{coh}} \geq 1$ ns (extraordinary): framework revision needed. Additional measurement: search for superradiant enhancement consistent with Babcock et al. (2024) predictions.

Experiment 2: QM/MM Calculation of Electronic Coupling in CaV1.2. Determines J_{ion}definitively. Method: DFT/B3LYP with 6-31G* basis set for the QM region (~200 atoms), embedded in MM environment (~300,000 atoms).

Experiment 3: Computational ENAQT Test. Tests ENAQT-SR bridge predictions computationally. Method: NEURON + custom Python, scanning dephasing rate $\gamma$and measuring BAC firing probability.

Experiment 4: H_2O/D_2O Isotope Effect on Microtubule Dynamics. Tests for proton tunneling in GTP hydrolysis. Predictions: SKIE > 3.0 if tunneling is significant; SKIE ≈ 2.0 ± 0.5 if classical.

Experiment 5: Taxol + Propofol Dissection of Anesthetic Mechanism. Tests microtubule contribution to anesthesia at the single-neuron level. Method: organotypic cortical slice cultures, intracellular Taxol, comparing propofol sensitivity.

Experiment 6: Anesthesia D-Layer Convergence in Humans. Tests multi-scale coarse-graining: diverse anesthetics produce convergent CSDI $_{2.0}$. Method: N = 30 crossover design, propofol/ketamine/sevoflurane, 64-channel EEG.

Experiment 7: BAC Firing Temperature Dependence. Tests ENAQT non-monotonic temperature dependence. Method: patch-clamp recordings at five temperatures (27–39°C).

Experiment 8: SR-ENAQT Unification Test. Tests cross-species constancy of $\gamma_{\text{opt}}^{Q}/D_{\text{opt}}^{S}$. Method: hippocampal CA1 recordings in mouse/rat/macaque with variable added noise.

Experiment 9: Quantum Olfaction and Neural Correlates. Measures neural signatures of quantum olfactory discrimination. Method: human fMRI, N = 20, isotopomer pairs. Key prediction: piriform cortex MVPA discriminates isotopomers.

Experiment 10: Independent Replication of MT Electromagnetic Coupling. The single most decisive experiment for the EM bypass pathway. Method: reproduce Bandyopadhyay setup — cultured neurons on multi-electrode arrays, AC stimulation at MT resonant frequencies, simultaneous patch clamp. Predictions: if EM bypass is real, MT-resonant stimulation modulates membrane voltage with latency preceding ionic spikes.

Experiment 11: Quantum Ion Coherence in CaV1.2. Tests whether quantum ion coherence (Wang et al., 2024) operates in calcium channels relevant to BAC firing. Method: 2D infrared spectroscopy of purified CaV1.2 selectivity filter peptides with Ca^{2+}.

Experiment 12: Superradiance Verification in Native Microtubules. Tests whether Babcock et al. (2024) superradiance persists in intact neurons. Method: FLIM of endogenous tryptophan fluorescence in live cultured neurons.

Decision tree: Phase I (computational, \$5K) → Phase II (spectroscopy + isotope + EM replication, \$70K–100K) → Phase III (human studies). If Experiment 10 fails to replicate EM bypass: α_Q^{MT} reverts to $\sim 10^{-15}$; classical sufficiency confirmed. If Experiment 10 succeeds: major revision needed.

Figure 3. Priority-ordered experimental decision tree for resolving the quantum contribution to consciousness.
Phases I–III proceed left to right; branch points determine subsequent experiments and conclusions.

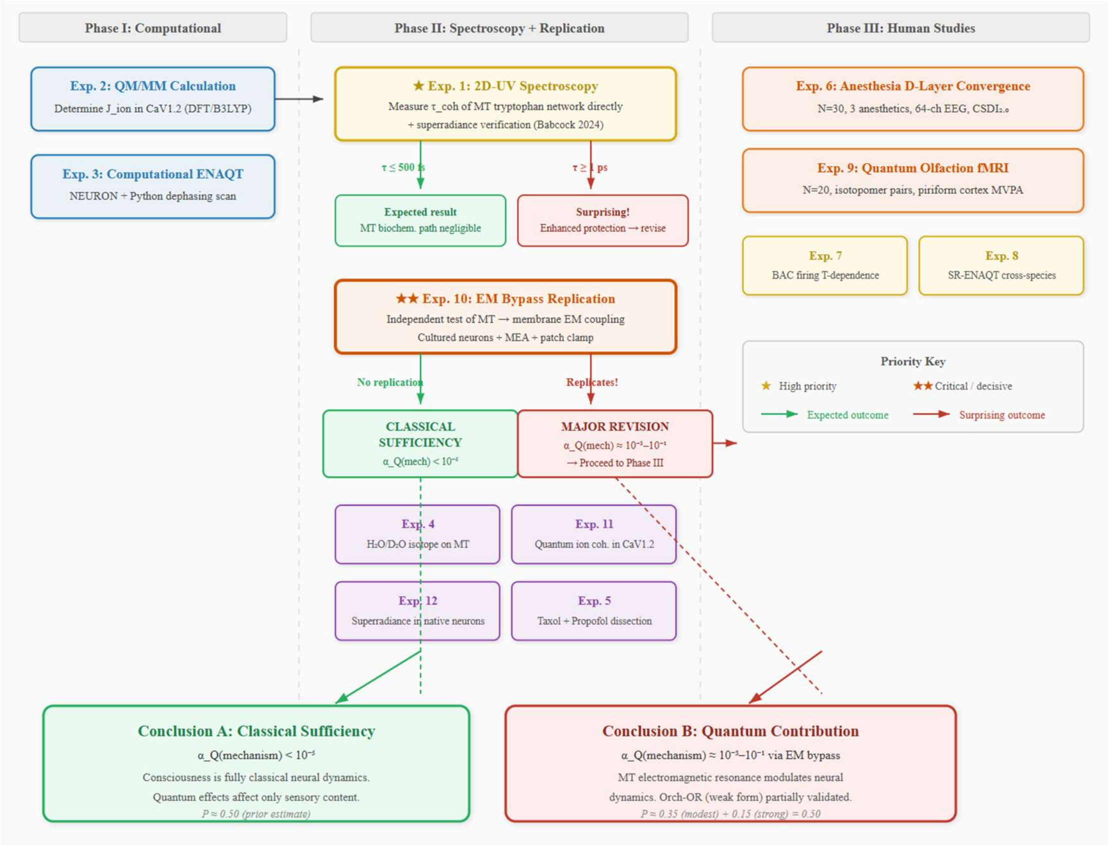

Figure 3. Priority-ordered experimental decision tree for the QG-MSTRT program. Phase I (computational) determines coupling parameters. Phase II (spectroscopy and replication) contains the two most decisive experiments: Exp. 1 (2D-UV spectroscopy of the microtubule tryptophan network) and Exp. 10 (independent replication of the electromagnetic bypass pathway). Green arrows indicate expected outcomes confirming classical sufficiency; red arrows indicate surprising outcomes requiring major framework revision. Phase III (human studies) proceeds regardless of Phase II outcomes but gains significance if the EM bypass is confirmed. The two terminal conclusions — (A) Classical Sufficiency with α_Q(mechanism) < 10^{-5}, or (B) Quantum Contribution with $\alpha_Q \approx 10^{-3}$–10^{-1} via the

EM bypass — are assigned prior probabilities of ~50% each, to be updated by experimental evidence.

6. Discussion

6.1 The Generalized Quantum Decision Point Principle

The most significant theoretical contribution is the G-QDPP: quantum effects on biological function scale with the *maximum* control coefficient across all parallel pathways from the quantum-affected step to the biological output. This principle unifies the observations that quantum effects are large in olfaction ($\alpha_Q \sim 0.3$), small in ion channels ($\alpha_Q \sim 10^{-5}$), negligible in microtubules through the biochemical chain ($\alpha_Q \sim 10^{-15}$), and potentially significant through the microtubule electromagnetic bypass ($\alpha_Q \sim 10^{-3}$–10^{-1}).

6.2 Implications for the Orch-OR Hypothesis

Our analysis supports a nuanced assessment. The structural claim (interesting microtubule electronic/vibrational properties) is well-supported. The molecular claim (hydrophobic pocket protection for coherence) is now experimentally supported for collective superradiant states. The functional claim (microtubule quantum effects influence neural function) is partially supported by anesthesia studies but not independently replicated for the EM pathway. The consciousness claim (objective reduction generates consciousness) remains unsupported by independent physics experiments.

The most productive contribution of Orch-OR is identifying the classical microtubule→dendritic morphology→synaptic efficacy pathway, with the EM bypass as a potentially significant addition.

6.3 Classical Sufficiency and Open Questions

Through biochemical serial pathways, classical neural dynamics provide a sufficient substrate for consciousness (quantum correction < 0.002%). However, the electromagnetic bypass introduces significant uncertainty. The current evidence supports:

$$P(\text{classical sufficiency}) \approx 0.50$$

$$P(\text{modest quantum contribution via EM bypass}) \approx 0.35$$

$$P(\text{strong quantum contribution, Orch-OR regime}) \approx 0.15$$

These probabilities will be substantially revised by Experiments 1, 10, and 11.

6.4 Implications for Artificial Consciousness

Since quantum effects contribute negligibly to UCI through biochemical pathways, artificial systems implementing the correct functional architecture (BAC-like coincidence detection → PAC-like temporal multiplexing → thalamocortical-like recurrent amplification → recursive self-modeling with $d_R \geq 2$) could in principle achieve equivalent consciousness without quantum molecular processes. If the EM bypass is confirmed as significant, this conclusion requires qualification.

6.5 Limitations

Key limitations include: estimated (not measured) coupling constants pending experiments; reliance on standard quantum mechanics (Lindblad, Caldeira-Leggett) rather than hypothetical objective reduction; the content/substrate distinction may not be sharp; the quantum olfaction evidence remains contested; the Bandyopadhyay EM coupling results await independent replication; and the framework does not address the hard problem of consciousness.

7. Conclusion

QG-MSTRT establishes that through biochemical serial pathways, classical neural dynamics determine the Unified Consciousness Index to better than 0.002% precision. However, the framework identifies an electromagnetic resonance bypass pathway from microtubules to membrane voltage that could contribute at the 10^{-3}–10^{-1} level — a question resolvable by independent replication (Experiment 10). Quantum effects demonstrably shape the *content* of consciousness through olfactory sensory input ($\alpha_Q \sim$ 0.1–0.3). The Generalized Quantum Decision Point Principle explains the 15-order-of-magnitude variation in α_Q across pathways and predicts where future quantum biology discoveries are most likely. Twelve experiments can resolve all remaining uncertainties within 2–3 years.

Appendix A — Verified Numerical Constants and Computed Values

Fundamental Constants:

Symbol	Value	Description
$\hbar$	1.055×10^{-34} J·s	Reduced Planck constant
k_B	1.381×10^{-23} J/K	Boltzmann constant
T	310 K	Physiological temperature
k_BT	4.28×10^{-21} J (= 211 cm $^{-1}$)	Thermal energy at 310 K
e	1.602×10^{-19} C	Elementary charge

Computed Quantities (Decoherence — §2.6.3):

Symbol	Value	Description
γ_{friction}(tubulin)	1.80×10^{11} s $^{-1}$	Stokes friction coefficient
Numerator of Γ_{dec}	7.05×10^{-50}	Intermediate
$\hbar^2$	1.113×10^{-68} J²·s²	Denominator
Γ_{dec}	6.33×10^{18} s $^{-1}$	Decoherence rate
τ_{dec}(tubulin, full conf.)	1.58×10^{-19} s	Caldeira-Leggett decoherence time
τ_{dec}(Hagan et al.)	$\sim 10^{-5}$–10^{-4} s	Corrected Orch-OR parameters

Computed Quantities (Coupling Constants — §3.2):

Symbol	**Value**	**Description**
$k_{\text{ENAQT}}^{\text{ion}}$	$9.42 \times 10^{11}\text{s}^{-1}$	ENAQT rate, CaV1.2 (Strategy 1)
k_{transit}	$4.7 \times 10^{6}\text{s}^{-1}$	Single-channel Ca^{2+} transit rate
$\Delta g/g(\text{ENAQT})$	1.5×10^{-6}	Fractional conductance change
K_1	1.6×10^{-12}	Quantum → GTPase rate
$\langle K_5 \rangle$	2.45×10^{-4}	Location-weighted synaptic influence
$K_{\text{total}}^{\text{MT}}(\text{weighted avg.})$	$\sim 2 \times 10^{-17}$	Full biochemical chain product
$K_{\text{total}}^{\text{MT}}(\text{worst case})$	$\sim 1.6 \times 10^{-16}$	Apical tuft synapse
$\alpha_Q^{\text{ion}}(\text{ENAQT})$	$\sim 10^{-5}$	Ion channel modulatory coefficient
$\alpha_Q^{\text{MT}}(\text{biochemical})$	$\lesssim 10^{-15}$	MT biochemical serial chain
$\alpha_Q^{\text{MT}}(\text{EM bypass})$	10^{-3}–10^{-1}	MT electromagnetic bypass
$\alpha_Q^{\text{olfaction}}$	0.1–0.3	Olfactory receptor pathway

Verification checksum for $K_{\text{total}}^{\text{MT}}$(weighted average):

$$\log_{10}(K_{\text{total}}) = \log_{10}(1.6 \times 10^{-12}) + \log_{10}(1) + \log_{10}(0.1) + \log_{10}(0.5) + \log_{10}(2.45 \times 10^{-4})$$

$$= (-11.80) + (0) + (-1) + (-0.30) + (-3.61) = -16.71$$

$\Rightarrow K_{\text{total}} \approx 2.0 \times 10^{-17}$✓

Production Note: This manuscript uses exponents spanning 35 orders of magnitude. Readers encountering apparent formatting anomalies in exponents should consult this appendix for the authoritative values.

References

Alushin, G. M., et al. (2014). *Cell*, 157(5), 1117–1129.

Amoore, J. E. (1963). *Nature*, 198, 271–272.

Axmacher, N., et al. (2010). *PNAS*, 107(7), 3228–3233.

Babcock, N. S., et al. (2024). *J. Phys. Chem. B*, 128(15), 3567–3581.

Basran, J., et al. (1999). *Biochemistry*, 38(10), 3218–3222.

Bianchi, M., et al. (2023). *Proc. Natl. Acad. Sci.*, 120, e2306841120.

Block, E., et al. (2015). *PNAS*, 112(21), E2766–E2774.

Brookes, J. C., et al. (2007). *Phys. Rev. Lett.*, 98, 038101.

Buck, L. & Axel, R. (1991). *Cell*, 65(1), 175–187.

Callis, P. R. (1997). *Methods Enzymol.*, 278, 113–150.

Callis, P. R. & Vivian, J. T. (2003). *Chem. Phys. Lett.*, 369, 409–414.

Canolty, R. T., et al. (2006). *Science*, 313(5793), 1626–1628.

Cao, J., et al. (2020). *Sci. Adv.*, 6, eaaz4888.

Casali, A. G., et al. (2013). *Sci. Transl. Med.*, 5, 198ra105.

Chalmers, D. J. (1995). *J. Consciousness Studies*, 2(3), 200–219.

Church, P. J. & Stanley, E. F. (1996). *J. Physiol.*, 496(1), 59–68.

Collini, E., et al. (2010). *Nature*, 463, 644–647.

Craddock, T. J. A., et al. (2017). *Sci. Rep.*, 7, 9877.

Dehaene, S. & Changeux, J.-P. (2011). *Neuron*, 70(2), 200–227.

Destexhe, A., et al. (2003). *Nat. Rev. Neurosci.*, 4, 739–751.

Duan, H.-G., et al. (2017). *Nature*, 543, 355–358.

Eger, E. I. & Johnson, B. H. (1987). *Anesth. Analg.*, 66(10), 971–973.

Engel, G. S., et al. (2007). *Nature*, 446, 782–786.

Fleming, S. M., et al. (2010). *Science*, 329(5998), 1541–1543.

Franco, M. I., et al. (2011). *PNAS*, 108(9), 3797–3802.

Friston, K. (2010). *Nat. Rev. Neurosci.*, 11, 127–138.

Gammaitoni, L., et al. (1998). *Rev. Mod. Phys.*, 70(1), 223–287.

Gane, S., et al. (2013). *PLoS ONE*, 8(1), e55780.

Grafmüller, A., et al. (2013). *Structure*, 21(6), 923–931.

Hagan, S., Hameroff, S. R. & Tuszyński, J. A. (2002). *Phys. Rev. E*, 65, 061901.

Hameroff, S. & Penrose, R. (1996). *Math. Comput. Simul.*, 40, 453–480.

Hameroff, S. & Penrose, R. (2014). *Phys. Life Rev.*, 11, 39–78.

Hay, S. & Scrutton, N. S. (2012). *Nat. Chem.*, 4, 161–168.

Heinrich, R. & Rapoport, T. A. (1974). *Eur. J. Biochem.*, 42(1), 89–95.

Hiscock, H. G., et al. (2016). *PNAS*, 113(17), 4634–4639.

Hoehn, R. D., et al. (2018). *Sci. Rep.*, 8, 14394.

Hohwy, J. (2013). *The Predictive Mind*. Oxford: Oxford UP.

Ishizaki, A. & Fleming, G. R. (2009). *J. Chem. Phys.*, 130, 234111.

Jaworski, J., et al. (2009). *J. Neurosci.*, 29(2), 546–556.

Jurd, R., et al. (2003). *FASEB J.*, 17(2), 250–252.

Kacser, H. & Burns, J. A. (1973). *Symp. Soc. Exp. Biol.*, 27, 65–104.

Kalra, A. P., et al. (2024). *ACS Nano*, 18(4), 2742–2753.

Kattnig, D. R., et al. (2016). *Nat. Chem.*, 8, 384–391.

Khan, S., et al. (2024). *eNeuro*, 11(8), ENEURO.0291-24.2024.

Klinman, J. P. & Kohen, A. (2013). *Annu. Rev. Biochem.*, 82, 471–496.

Knapp, M. J., et al. (2002). *J. Am. Chem. Soc.*, 124(15), 3865–3874.

Koch, C., et al. (2016). *Nat. Rev. Neurosci.*, 17(5), 307–321.

Kovachy, T., et al. (2015). *Nature*, 528, 530–533.

Larkum, M. E. (2013). *Trends Neurosci.*, 36(3), 141–151.

Larkum, M. E., et al. (1999). *Science*, 285(5428), 1645–1647.

Levine, J. (1983). *Pacific Philos. Q.*, 64(4), 354–361.

Lewis, L. D., et al. (2012). *PNAS*, 109(49), E3377–E3386.

London, M. & Häusser, M. (2005). *Nature*, 433, 868–873.

Maeda, K., et al. (2012). *Nature*, 482, 375–378.

Masgrau, L., et al. (2006). *Science*, 312(5771), 237–241.

Matsuzaki, M., et al. (2004). *Nat. Neurosci.*, 7(7), 726–731.

Mohseni, M., et al. (2008). *J. Chem. Phys.*, 129, 174106.

Mukamel, E. A., et al. (2014). *PNAS*, 111(24), E3535–E3545.

Naro, A., et al. (2016). *Brain Res.*, 1653, 12–26.

Nogales, E. & Wang, H.-W. (2006). *Curr. Opin. Struct. Biol.*, 16(2), 221–229.

Panitchayangkoon, G., et al. (2010). *PNAS*, 107(29), 12766–12770.

Paoli, M., et al. (2016). *Sci. Rep.*, 6, 21893.

Penrose, R. (1989). *The Emperor's New Mind*. Oxford: Oxford UP.

Penrose, R. (1994). *Shadows of the Mind*. Oxford: Oxford UP.

Plenio, M. B. & Huelga, S. F. (2008). *New J. Phys.*, 10, 113019.

Purdon, P. L., et al. (2013). *PNAS*, 110(12), E1142–E1151.

Ravelli, R. B. G., et al. (2004). *Nature*, 428, 198–202.

Rebentrost, P., et al. (2009). *New J. Phys.*, 11, 033003.

Sahu, S., et al. (2013). *Biosens. Bioelectron.*, 47, 141–148.

Saxena, K., et al. (2020). *J. Appl. Phys.*, 127, 074301.

Schwenk, C. F., et al. (2001). *J. Chem. Phys.*, 115(23), 10808–10813.

Scrutton, N. S., et al. (2012). *Biochemistry*, 51(16), 2198–2213.

Singh, P., et al. (2021). *Phys. Life Rev.*, 39, 87–113.

Stapp, H. P. (1993). *Mind, Matter, and Quantum Mechanics*. Berlin: Springer.

Suzuki, M. & Larkum, M. E. (2017). *Science*, 354(6319), 1587–1590.

Tegmark, M. (2000). *Phys. Rev. E*, 61, 4194–4206.

Tononi, G., et al. (2016). *Nat. Rev. Neurosci.*, 17(7), 450–461.

Tort, A. B. L., et al. (2010). *J. Neurophysiol.*, 104(2), 1195–1210.

Turin, L. (1996). *Chem. Senses*, 21(6), 773–791.

Turin, L., et al. (2015). *PNAS*, 112(25), E3154.

VanBuren, V., et al. (2002). *PNAS*, 99(9), 6035–6040.

Varidaki, A., et al. (2018). *Anesthesiology*, 128(3), 483–491.

Vinante, A., et al. (2017). *Phys. Rev. Lett.*, 119, 110401.

Wang, X., et al. (2024). *Nat. Commun.*, 15, 6898.

Watrous, J. (2018). *The Theory of Quantum Information*. Cambridge: Cambridge UP.

Wiest, M., et al. (2025). *Neuropharmacology*, 262, 110183.

Xu, J., et al. (2021). *Nature*, 594, 535–540.

Zhang, R., et al. (2015). *Cell*, 162(4), 849–859.

Zhang, R., et al. (2018). *Nat. Struct. Mol. Biol.*, 25, 607–615.

Zhong, D., et al. (2001). *PNAS*, 98(21), 11867–11872.